WorId Ocean Circulation Experiment

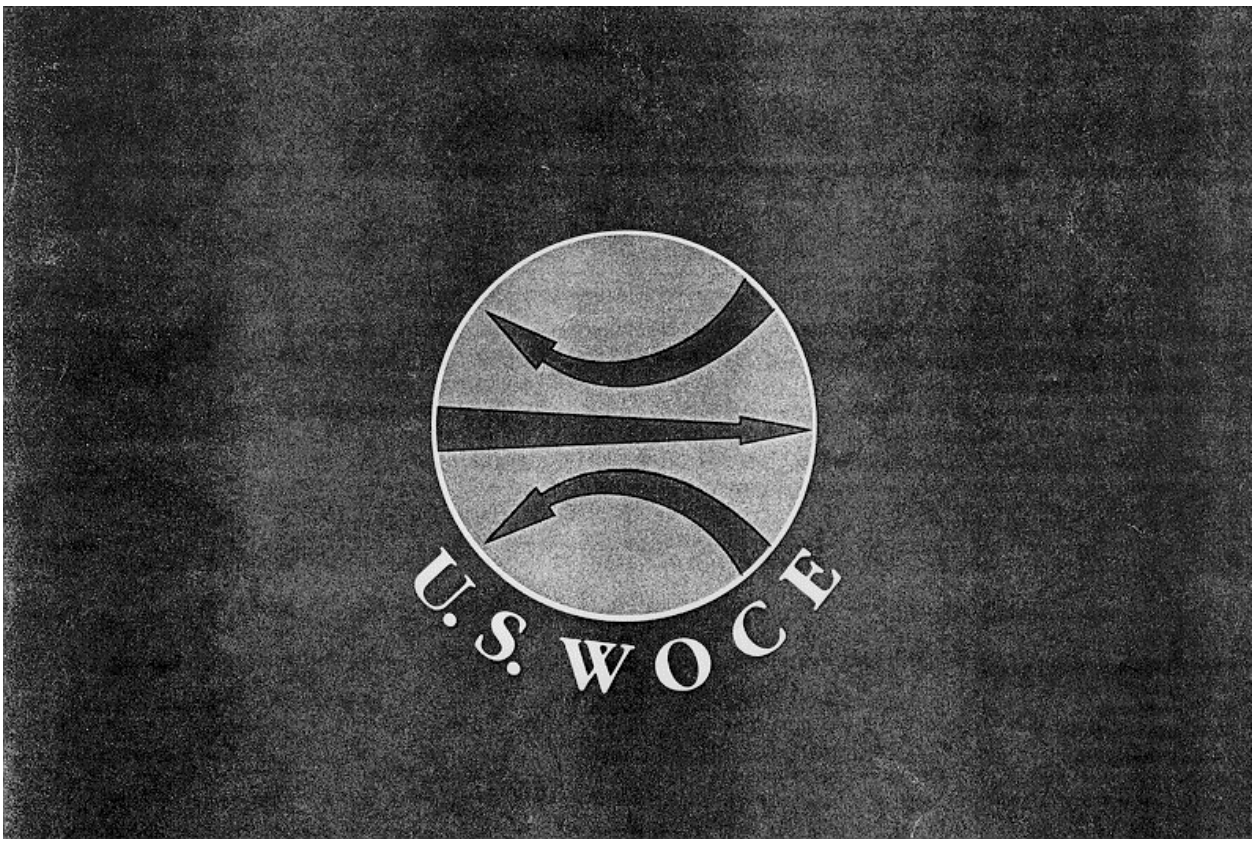

WOCE/NASA Altimeter Algorithm Workshop

U.S. WOCE Technical Report
Number 2
November, 1988

This report may be cited as:

Chelton, Dudley B., WOCE/NASA Altimeter Algorithm Workshop, U.S. WOCE Technical Report No. 2, 70 pp., U.S. Planning Office for WOCE, College Station, TX 1988.

WORLD OCEAN CIRCULATION EXPERIMENT

U.S. WOCE Technical Report Number 2

WOCE/NASA Altimeter Algorithm Workshop

Oregon State University
Corvallis, Oregon
August 24–26, 1987

by

Dudley B. Chelton
College of Oceanography
Oregon State University
Corvallis, Oregon 97331

on behalf of the

U.S. Science Steering Committee for WOCE

PREFACE

This is a report of a workshop held at Oregon State University, Corvallis, Oregon, in August 1987 to assess the accuracies of geophysical algorithms involved in altimeter data processing. New developments in satellite altimetry have made it possible to measure sea surface elevation to an unprecedented accuracy of a few centimeters. Several satellite altimeter missions are planned in the 1990s, and their success is vital to the WOCE goal of collecting the data needed to obtain a better understanding of the world ocean circulation. The workshop sought to establish an early dialogue between the scientists who will use the altimeter data and the engineers responsible for instrument design and algorithm implementation.

We hope the report of this workshop will further improvements in altimeter algorithms. We thank the workshop participants and especially Dr. Dudley Chelton, who chaired the workshop and authored this report, including the introductory chapter on the fundamentals of satellite altimetry. A companion volume, available on request from the U.S. WOCE Office, contains the text of the 42 papers on satellite altimetry submitted by workshop participants and others. The workshop was sponsored by the National Aeronautics and Space Administration and arranged through the U.S. Planning Office for WOCE.

U.S. WOCE Science Steering Committee
November 1988

FOREWORD

Satellite altimeter measurements of sea surface elevation, from which surface geostrophic currents can be inferred, are the only means by which the surface geostrophic circulation can be measured globally for long periods of time. Over the next four years, three new satellite altimeters will be launched into space for ocean circulation research applications. The European Space Agency has a scheduled launch in mid-1990 for the ERS-1 satellite, which includes an altimeter in its suite of four instruments. The U.S. National Aeronautics and Space Administration (NASA) and the French Centre National d'Etudes Spatiale (CNES) will jointly launch two altimeters on the dedicated TOPEX/POSEIDON altimetric mission in the early- to mid-1992 time frame. These three new altimeters follow a long heritage of satellite altimeters, beginning with SKYLAB in 1973, followed by GEOS-3 (April 1975–December 1978) and SEASAT (July–October 1978). Presently, the GEOSAT altimeter has been providing useful altimetric measurements since March 1985. The ERS-1 and TOPEX/POSEIDON altimeters are important elements of the observational program of the World Ocean Circulation Experiment.

Over the time span since the SKYLAB altimeter, technological developments have transformed satellite radar altimetry from a technique by which major geoid features with order 10 m amplitude could be resolved to one where resolution of dynamic ocean signals as small as a few cm is possible. These improvements in the accuracy of satellite altimeter height measurements are among the most significant technological advancements that have made possible the global perspective of WOCE. The ERS-1 and TOPEX/POSEIDON altimeter missions will overlap the extensive WOCE *in situ* observational program. The combination of altimetric data with *in situ* observations and modeling through data assimilation promises significant advances toward understanding of global ocean circulation and its relation to short-term climate variations.

The high degree of accuracy required for altimetric studies of ocean circulation pushes the limits of present technology. A workshop to evaluate the accuracies of altimeter algorithms was held at Oregon State University in Corvallis, Oregon, on August 24–26, 1987. By its nature, satellite altimetry is a very multi-disciplinary technique for observing the ocean. To obtain centimetric accuracy of altimetric range measurements requires careful consideration of technical details of the instrumentation, atmospheric radiative transfer, the interaction of electromagnetic radiation with the sea surface, and a host of geophysical processes affecting the sea surface topography that are not related to the geostrophic currents of interest. To compound the problem, communication between altimeter instrumentation experts and the scientists who ultimately use the data is not as open as it could be. At one extreme, engineers sometimes have a difficult time appreciating the requirement for centimetric accuracy. At the other, many scientists have little concern or appreciation for the technical details of altimetry. One of the goals of the workshop was to establish a dialogue between the engineers and scientists who share a common interest in the success of satellite altimetry.

The focus of the workshop was on the geophysical algorithms for the altimeter measurements of height and normalized radar cross section $\sigma^{\bullet}$. Some of the sensor algorithms directly relevant to the geophysical algorithms were also considered. Algorithms for significant wave height were not considered at the workshop. A total of 36 presentations were given, including overviews of the SEASAT, GEOSAT, ERS-1, and TOPEX/POSEIDON altimeters and summaries of individual algorithms. Written summaries of these presentations are included in the proceedings of the workshop, published as a separate volume Appendix to U.S. WOCE Technical Report Number 2. Following these presentations, participants broke up into four working groups to discuss the present status of each algorithm and address the following specific issues:

1) is there a clear physical basis for the algorithm?
2) does the algorithm differ for the different altimeters and, if so, why?
3) are there any potential or known problems with the algorithm?
4) can implementation of the algorithm be tested for accuracy and validity?
5) what recommendations can be made for the algorithm?

At the end of the workshop, the working group chairmen provided written summaries of the working group discussions and recommendations for each algorithm. Edited versions of these summaries are included in this report. Some of the algorithm recommendations listed in this summary have evolved out of other meetings and discussions that have taken place since the time of the workshop. Also included here is a tutorial of the fundamentals of satellite altimetry with summaries of the physical basis for each algorithm.

ACKNOWLEDGMENTS

We thank George Born, Philip Callahan, Trevor Guymer and Meric Srokosz for chairing the working groups and contributing much of the discussion in Secs. 3–6 of this report. George Born and Donna Witter helped with the writing of Sec. 2.6.4. We especially thank George Born, Lee-Lueng Fu and Ted Strub for their thorough, constructive, and quick reviews of an earlier draft of this report.

Financial support for the WOCE/NASA Altimeter Algorithm Workshop was provided by the U.S. National Aeronautics and Space Administration. The workshop summary was prepared with support from NASA Grant NAGW-730 and Contract 958127 from the Jet Propulsion Laboratory funded under the NASA TOPEX/POSEIDON Announcement of Opportunity.

TABLE OF CONTENTS

Page

1. INTRODUCTION

Satellite altimetry is relatively unique among spaceborne oceanographic remote sensing techniques in that it has spanned more than one and a half decades of experience. There has been an orderly transition from one generation of altimeters to the next, with significant improvements in measurement precision and accuracy with each new altimeter. The first dedicated altimetric mission was GEOS-3 (April 1975 to December 1978), with a measurement precision of 25 cm in 1-s averages (Stanley *et al.*, 1979). Technological improvements increased this measurement precision for 1-s averages to about 5 cm for the SEASAT altimeter (Tapley *et al.*, 1982a) which operated from July to October 1978. Further improvements have resulted in better than 5 cm precision on the presently operational (since March 1985) GEOSAT altimeter (Sailor and LeSchack, 1987). The lack of an on-board microwave radiometer for estimating atmospheric water vapor range delays, however, has somewhat degraded the overall accuracy of the GEOSAT measurements compared with SEASAT. Nonetheless, a number of interesting scientific results have already been obtained from GEOSAT data.

The ERS-1 altimeter, with an anticipated launch in mid-1990, is expected to have a measurement precision comparable to GEOSAT, but with improved accuracy from the addition of a water vapor microwave radiometer. The biggest improvements in measurement precision and accuracy will be with the next-generation TOPEX and POSEIDON altimeters scheduled to be launched jointly in 1991. The POSEIDON altimeter will incorporate the first totally solid state transmitter. The low power requirements and low cost of solid state transmitters could significantly reduce the costs of future altimeters. The TOPEX altimeter incorporates a dual-frequency transmitter (one of which will be solid state) with the ambitious goal of achieving a measurement precision of better than 4 cm in 1-s averages, an orbit height accuracy of 13 cm, and accuracies of better than 2 cm each for all corrections applied to the height measurements (TOPEX Science Working Group, 1981). The overall error budget represents nearly an order of magnitude improvement over previous altimeters (mostly due to the reduced orbit error).

The technique by which sea surface elevation signals of oceanographic origin are estimated from raw altimetric measurements is very complex. A total of approximately 60 algorithms are involved in conversion from telemetered units to engineering and geophysical units, corrections for instrumental effects, corrections for atmospheric effects, and removal of external geophysical signals that are not related to the oceanographic signals of interest. These algorithms can be classified as sensor algorithms or geophysical algorithms. The sensor algorithms correct the altimeter measurements for instrument-related biases. This involves the use of pre- and post-launch calibration data, instrumental measurements (e.g., temperatures of the components), and table look-up formulations of corrections. The geophysical algorithms convert the sensor data to the geophysical quantities of interest (sea surface elevation, significant wave height, and normalized radar cross section).

The purpose of the WOCE/NASA Altimeter Algorithm Workshop was to review the present status of each of the geophysical algorithms. In addition, a selected few sensor algorithms were included because of their importance to the overall height measurement error budget. The discussion was limited to the algorithms relevant to measurements of height and normalized radar cross section; algorithms for altimeter estimates of significant wave height were not considered. Detailed descriptions of each of the algorithms considered were presented before the general audience during the first two days of the workshop. On the third day of the workshop, participants broke up into four working groups to discuss in detail the present status of each of the algorithms considered. A list of the four working groups, the working group chairmen, and the algorithms considered by each working group is given in Table 1. The conclusions and recommendations of the four working groups are summarized in Secs. 3–6 of this workshop summary. Some of the recommendations listed in this summary have evolved out of other meetings and discussions that have taken place since the time of the workshop. Also included here in Sec. 2 is a summary of the fundamentals of satellite altimetry and overviews of the physical basis for each of the geophysical algorithms.

In addition to the specific recommendations listed in Secs. 3–6 for each algorithm, the workshop participants made the following general recommendations to enhance the value of geophysical data from the various satellite altimeters:

1) All altimeter projects should use common correction algorithms wherever possible.

2) All algorithms should be clearly documented, including rigorous error analyses.

3) Wherever practical, more than one source of geophysical corrections should be included in the geophysical data records, e.g., tides, geoid, sea level pressure, water vapor, ionospheric electrons, etc.

4) Quantitative error estimates of each correction should be provided wherever practical.

It is highly desirable for the error description to go beyond the usual one standard deviation specification to also include wavenumber-frequency characteristics.

2. FUNDAMENTALS OF SATELLITE ALTIMETRY

From an oceanographic perspective, the primary purpose of satellite altimetry is to measure the sea surface elevation resulting from dynamic ocean currents. A schematic summary of altimeter measurements and the corrections that must be applied to obtain the dynamic sea surface elevation is given in Fig. 1. The altimeter transmits a short pulse of microwave radiation with known power toward the sea surface at satellite nadir (the

point directly beneath the satellite). This pulse interacts with the sea surface and part of the incident radiation reflects back to the satellite. The range from the satellite to the sea surface can be determined from the 2-way travel time of the pulse. In addition, near-surface wind speed and significant wave height can be determined from the power and shape of the returned signal. The methods used to estimate these three geophysical quantities are summarized in this section.

2.1 Normalized Radar Cross Section and Wind Speed

At the microwave frequencies of interest to satellite altimetry (5–15 GHz), the reflectivity (fraction of incident radiation reflected) of the sea surface is 0.6–0.7 (Maul, 1985, Fig. 2.21). Thus, for a smooth sea surface, a large fraction of incident radiation reflects back in the direction of the satellite. As the sea surface roughness increases, more of the incident radiation is reflected in directions away from the satellite and the power of the return signal received by the altimeter decreases. The power of the received signal is expressed as the normalized radar cross section $\sigma^\bullet$, which is proportional to the ratio of received to transmitted power normalized by the area illuminated by the radar pulse (Skolnik, 1970; Stewart, 1985; Chelton and Wentz, 1986). For accurate measurements of radar backscatter, 2-way attenuation by the atmosphere must be considered. Attenuation by rain droplets is large. Altimeter measurements contaminated by rainfall are generally flagged (based on independent microwave radiometer estimates of rain rate, see e.g. Wilheit *et al.*, 1978; Alishouse, 1983) and excluded from subsequent analysis. Except in the presence of very dense clouds or water vapor, the atmospheric transmittance in non-raining conditions is greater than 0.97 at altimeter transmitted microwave frequencies of 5–15 GHz (Maul, 1985, Table 5.7). The 2-way attenuation correction to $\sigma^\bullet$ in rain-free conditions is therefore typically less than 5% and is generally ignored.

TABLE 1 List of working groups, working group chairmen, and algorithms addressed by the WOCE/NASA Altimeter Algorithm Workshop.

Backscatter and Wind Speed Algorithms (Chairman: Trevor Guymer)

1. backscatter algorithms
2. wind speed algorithms

Instrument and Air-Sea Interface Algorithms (Chairman: Meric Srokosz)

1. tractor algorithms
2. EM and skewness biases
3. antenna mispointing error
4. gain calibration

Atmospheric Refraction Corrections (Chairman: Philip Callahan)

1. ionospheric correction
2. dry tropospheric correction
3. wet tropospheric correction

External Physical Corrections (Chairman: George Born)

1. ocean and solid earth tides
2. static inverse barometer
3. geoid
4. precision orbit determination
5. height bias residual

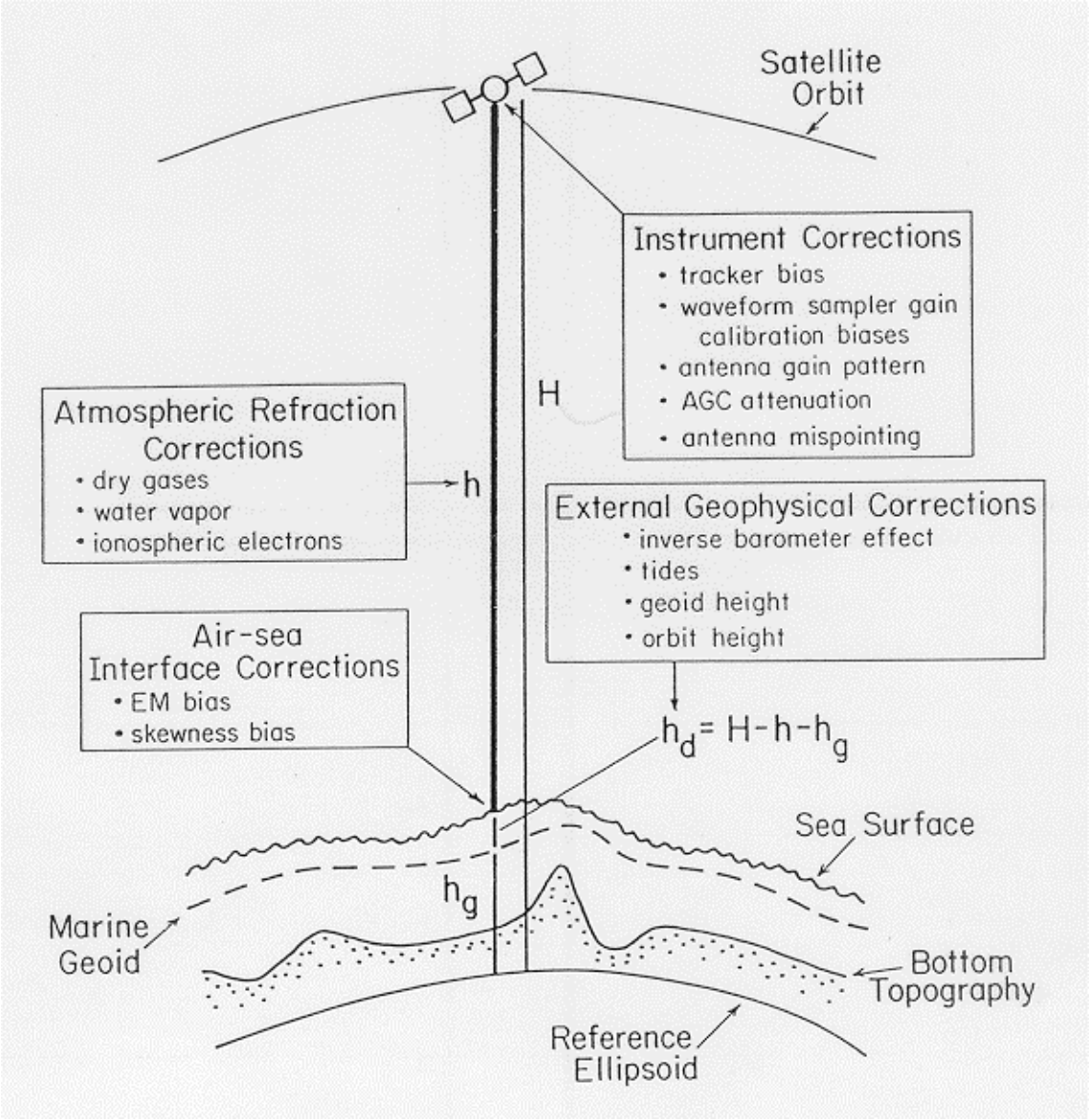

Figure 1. A schematic summary of altimeter measurements and the corrections that must be applied to obtain the dynamic sea surface elevation h_d. The altimeter range measurement is h, and H and h_g are the orbit height and geoid height, respectively, relative to a reference ellipsoid approximation to the earth's surface.

The nature of radar power backscattered from the sea surface depends strongly on the incidence angle of the radiation (Moore and Fung, 1979; Barrick and Swift, 1980). At the small incidence angles relevant to satellite altimetry (less than a few degrees from satellite nadir), the backscattered radiation results primarily from specular reflection from the portion of the surface wave spectrum with wavelengths longer than the incident radiation (about 2.2 cm for a 13.5 GHz radar altimeter). As the wind speed increases, the sea surface roughness increases and a greater fraction of the incident radiation is reflected away from the satellite. Thus, at incidence angles near nadir, the power of the backscattered radiation is inversely related to wind speed but independent of wind direction. The normalized radar cross section σ• could be determined to a high degree of accuracy from geometrical optics given the wavenumber spectrum of the sea surface and the wavelength of the radiation (Barrick and Bahar, 1986; Jackson *et al.,* 1988).

The difficulty in estimating wind speed from a radar altimeter lies in relating the surface roughness to near-surface winds. Over the past two decades there have been several attempts to develop model functions for estimating wind speed directly from near-nadir measurements of σ•. These model functions have ranged from purely theoretical (Barrick, 1974; Barrick and Bahar, 1986; Jackson *et al.,* 1988), to partly theoretical (Brown, 1979; Brown *et al.,* 1981; Mognard and Lago, 1979), to purely empirical (Chelton and McCabe, 1985; Chelton and Wentz, 1986; Dobson *et al.,* 1987). The empirical model functions have generally been the most successful, largely because the theoretical formulation is not yet fully understood. To first order, the relation between σ• in dB and the wind speed $u_{19.5}$ in m/s measured at 19.5 m above the sea surface is

$$\sigma^{\circ}(dB) = 10\left[A + B\log_{10} u_{19.5}\right] \qquad \text{(l)}$$

where A and B are approximately 1.5 and –0.47, respectively, for 0• incidence angle (Chelton and McCabe, 1985). The danger of purely empirical formulations is that important physical processes that might influence the σ• measurements are hidden in the model functions. An improved theoretical understanding of the physics of nadir radar backscatter will shed light on the strengths and limitations of satellite altimeter estimates of sea surface wind speed.

2.2 Automatic Gain Control

In practice, σ• is not measured directly by the altimeter. In order to operate the altimeter electronics within the linear response region of all receiver stages, an automatic gain control (AGC) loop is implemented in the electronics package (Townsend, 1980). The AGC determines the attenuation that must be applied to the returned signal to keep constant the total power of the return signal measured by the altimeter. The altimeter transmits and receives 1000 or more pulses per second. To reduce geophysical Rayleigh noise in individual received pulses (see discussion in Sec. 2.4), the AGC loop averages all individual waveforms received over 1/20 s to determine the appropriate attenuation

value. This AGC value is transmitted to the ground for radar cross section processing. The stepsize of the telemetered AGC values was 1/16 dB for SEASAT and GEOSAT in a 10/s telemetry string and will be 1/4 dB for TOPEX in a 20/s telemetry string. The normalized radar cross section σ° is computed from the AGC value, with corrections for loss from variations in satellite altitude and non-zero antenna pointing angle due to pitch, roll, and yaw of the satellite (see Chelton and McCabe, 1985). The coarse step size in the telemetered AGC values limits the precision of the σ° estimates. For SEASAT, the σ° precision in 1-s averages was 0.3 dB (Chelton and McCabe, 1985). With the underlying nonlinear relationship (1) between σ° and wind speed, this corresponds to a wind speed precision of 1–4 m/s, depending on wind speed.

2.3 Atmospheric Refraction

Estimation of the range from the satellite to the sea surface (shown as h in Fig. 1) is conceptually straightforward. Defining t_0 to be the 1-way travel time (equal to half of the measured 2-way travel time), the range is

$$h = \int_0^{t_0} c\, dt, \tag{2a}$$

where c is the speed of light, which varies along the path between the satellite and the sea surface. For a perfect vacuum, the speed of light is equal to a constant $c_0 = 2.998 \times 10^8$ m/s. Ignoring atmospheric refraction, the range from the satellite to the sea surface would be related to the 1-way travel time t_0 by

$$h_0 = \int_0^{t_0} c_0\, dt = c_0\, t_0. \tag{3}$$

The actual speed of light is related to the real part of the index of refraction η by $c = c_0/\eta$. The actual range is therefore

$$h = \int_0^{t_0} \frac{c_0}{\eta}\, dt. \tag{2b}$$

Since η is greater than 1, the actual range h *is* less than the value h_0 obtained from t_0 ignoring atmospheric refraction. The range correction to account for atmospheric refraction is

$$\Delta h = h_0 - h = \int_0^{t_0} \frac{c_0}{\eta}(\eta - 1) dt \tag{4a}$$

Atmospheric refraction is generally expressed in terms of the refractivity N, defined as $N = 10^6(\eta - 1)$. Since travel time and path length are related by $dz = c_0/\eta\, dt$, the range correction can be expressed in terms of distance along the path of the radar pulse by

$$\Delta h = 10^{-6} \int_0^{t_0} N(z)dz\,. \tag{4b}$$

The total atmospheric refractivity can be decomposed into contributions from dry gases (primarily oxygen), water vapor, liquid water (clouds), and ionospheric free electrons,

$$N = N_{\text{dry}} + N_{\text{vap}} + N_{\text{liq}} + N_{\text{ion}}\,. \tag{5}$$

The refractivities N_{dry}, N_{vap} and N_{liq} have all been determined empirically in terms of atmospheric properties. The refractivity N_{ion} can be determined from Maxwell's equations. Each of the four components of the range correction to account for atmospheric refraction is discussed briefly below.

2.3.1 Dry Tropospheric Range Correction

The refractivity of tropospheric dry gases is given to an accuracy of 0.2% by

$$N_{\text{dry}}(z) = 77.6\,P(z)/T(z) \tag{6a}$$

(Smith and Weintraub, 1953), where P is atmospheric pressure in mb and T is temperature in •K. Using the ideal gas law, this can be expressed as

$$N_{\text{dry}}(z) = 77.6\,R\rho(z), \tag{6b}$$

where R = 2.8704×10^6 ergs/(gm•K) is the universal gas constant and ρ is the density of dry gases. The dry tropospheric range correction is therefore

$$\Delta h_{\text{dry}} = 10^{-6} \int_0^h N_{\text{dry}}(z) = 77.6 \times 10^{-6}\, R \int_0^h \rho(z)dz\,. \tag{7a}$$

From the hydrostatic equation, the vertical integral of density is related to the surface atmospheric pressure P_0 and gravitational acceleration g by

$$P_0 = \int_0^\infty g(z)\rho(z)dz\,. \tag{8}$$

Most of the mass of the atmosphere is at altitudes lower than the height h of the satellite so that the integral in (8) can be approximated by an integral from the sea surface to

height *h*. In addition, the gravitational acceleration *g* is approximately constant over the altitude range from the sea surface to the height *h* and can therefore be removed from the integrand in (8) to a close degree of approximation. The dry tropospheric range correction in cm can therefore be approximated by

$$\Delta h_{\text{dry}} \approx 77.6 \times 10^{-6} R P_0 / g, \tag{7b}$$

where *R* is given above, *g* is in cm/s^2, and P_0 is in mb.

Thus, as first pointed out by Saastamoinen (1972), the dry tropospheric range delay is proportional to sea level pressure. In practice, a latitudinal dependence of g is used in (7b). For a value of *g* = 9S0.7 cm/s^2, the dry tropospheric range correction in cm in terms of sea level atmospheric pressure P_0 in mb is •h_{dry} = 0.2271 P_0. The sea level pressure must be obtained from meteorological model analyses which have errors that vary geographically and seasonally in ways that are difficult to quantify. The rms uncertainty of meteorological analyses of sea level pressure has been estimated to be approximately 3 mb in the northern hemisphere (TOPEX Science Working Group, 1981); the uncertainty is undoubtedly larger in the southern hemisphere. The dry tropospheric range correction is large (approximately 230 cm) but is only moderately sensitive to errors in sea level pressure; an error of 3 mb corresponds to a range error of only about 0.7 cm. Except in intense storms or high southern latitudes which are not well described by meteorological analyses, the dry tropospheric range delay is therefore generally a small source of error in altimeter range estimates.

2.3.2 Wet Tropospheric Range Correction

The refractivity of water vapor is given to an accuracy of better than 0.5~o by

$$N_{\text{vap}}(z) = 3.73 \times 10^5 e(z) / T^2(z) \tag{9a}$$

(Smith and Weintraub, 1953), where *T* is temperature in •K and *e* is the partial pressure of water vapor. The partial pressure of water vapor is related to the water vapor density *V* in gm/cm^3 by $e = 4.619 \times 10^3 VT$. The refractivity of water vapor can thus be expressed as

$$N_{\text{vap}}(z) = 1.723 \times 10^9 V(z) / T(z). \tag{9b}$$

The water vapor range correction in cm is therefore

$$\Delta h_{\text{vap}} = 10^{-6} \int_0^h N_{\text{vap}}(z) dz = 1723 \int_0^h \frac{V(z)}{T(z)} dz. \tag{10a}$$

The water vapor density decreases approximately exponentially with height in the atmosphere, with most water vapor generally in the lower 2 km of the atmosphere (Staelin *et al.,* 1976; Liu, 1984b). Defining T_{eff} to be the effective temperature over the height of significant water vapor, the water vapor range correction in cm can be expressed as

$$\Delta h_{\text{vap}} \approx \frac{1.723}{T_{eff}} \int_0^h V(z)dz \qquad (10b)$$

where T_{eff} is in •K and the vertically integrated water vapor density is in gm/cm^2.

The water vapor range delay is thus proportional to the vertically integrated water vapor density. Globally, this integral ranges from 1–6 gm/cm^2 (Chelton *et* al., 1981) and varies geographically and temporally over a broad range of time scales. The vertically integrated water vapor density can be estimated with an accuracy of approximately 0.3 gm/cm^2 from passive microwave measurements at two frequencies near the water vapor absorption line at 22.2 GHz (Tapley *et al.,* 1982b; Alishouse, 1983; Chang *et al.,* 1984). An uncertainty of 0.3 gm/cm^2 in the vertically integrated water vapor density results in an uncertainty of about 2 cm in the wet tropospheric range delay. Alternatively, the vertically integrated water vapor required for the wet tropospheric range correction can be obtained from meteorological model analyses. These models do not resolve spatial scales shorter than about 2000 km (Fu, personal communication) and have errors that vary geographically and seasonally in ways that are difficult to quantify. The uncertainty of water vapor values from meteorological analyses has been estimated to be about a factor of two larger than errors in microwave radiometer estimates of water vapor (Tapley *et al.,* 1982b), corresponding to an uncertainty of about 5 cm in the wet tropospheric range delay. Errors in meteorological models of atmospheric water vapor are likely larger in the southern hemisphere.

Another source of error in the wet tropospheric range correction is uncertainty in the value of T_{eff} in (l0b). The multiplicative factor for the vertically integrated water vapor varies from 6.15 to 6.38 for values of T_{eff} from 280•K to 270•K. For a multiplicative factor of 6.25, the water vapor range correction ranges from about 6 to 38 cm for vertically integrated water vapor values of 1–6 gm/cm^2. Uncertainty in the appropriate value of T_{eff} introduces a 2–4% uncertainty in the range correction.

The range delay introduced by liquid cloud droplets in the atmosphere can be described in terms of an effective refractivity derived using Mie scattering theory. Based on measurements of liquid drop size distribution over land, the effective refractivity N_{liq} has been found to be very nearly a linear function of the liquid droplet density *L(z).* An empirical expression (Resch, 1984) for N_{liq} in terms of the liquid water density in gm/cm^3 is

$$N_{\text{liq}}(z)d = 1.5L(z). \tag{11}$$

The coefficient in this expression is uncertain possibly by as much as a factor of two.

The range correction in cm due to liquid water droplets is therefore

$$\Delta h_{\text{liq}} = 10^{-6}\int_0^h N_{\text{liq}}(z)dz = 1.5\times 10^{-6}\int_0^h L(z)dz, \tag{12}$$

where the vertically integrated liquid water density is in gm/cm^2. For non-raining clouds, the liquid water density ranges from 1–4×10^{-6} gm/cm^3, but rarely exceeds 2.5×10^{-6}gm/cm^3 (Maul, 1985, p. 434). For a cloud thickness of 1 km, this corresponds to a vertically integrated liquid water density of 0.25 gm/cm^2. The corresponding liquid water range correction is 0.38 cm. The vertically integrated liquid water density can be estimated from passive microwave measurements at frequencies between 30 and 40 GHz for use in a liquid water range correction (Chang and Wilheit, 1979; Wentz, 1982; Alishouse, 1983). However, even if the multiplicative factor in (10) is in error by a factor of two, the liquid water range delay rarely exceeds 1 cm and is therefore generally ignored.

2.3.3 Ionospheric Range Correction

Atmospheric refraction from free electrons and ions in the upper atmosphere is related to the dielectric properties of the ionosphere. For electromagnetic radiation with frequencies greater than 1 GHz, the real part of the index of refraction η can be shown to be

$$\eta = \left(1 - f_p^2 / f^2\right)^{\frac{1}{2}} \tag{13a}$$

(Ginzburg, 1964), where f is the frequency of the transmitted signal and f_p is the plasma frequency, which represents the natural frequency of oscillation of electrons and ions in the atmosphere. The plasma frequency depends only on the electron density E and is given by $f_p^2 = \alpha E$ (Ginzburg, 1964), where E *is* in units of cm^{-3} and the constant α = 80.6 × 10^6 cm^3/s^2. For an electron density of 10^6 cm^{-3} typical of the ionosphere, f_p is approximately 9 MHz. Using the binomal expansion, the index of refraction for high frequencies f can be approximated by

$$\eta \approx 1 - \frac{f_p^2}{2f^2} = 1 - \frac{\alpha E}{2f^2}. \tag{13b}$$

The phase velocity of propagating electromagnetic radiation in the ionosphere is

$$cp = \frac{c_0}{\eta} = \frac{c_0}{1 - \alpha E / f^2}. \tag{14}$$

The propagation is thus dispersive with phase speeds exceeding c_0. The pulse transmitted by the altimeter propagates at the group velocity, which is given by

$$c_g = \frac{c_0}{\eta'} \tag{15}$$

where , η' is the group index of refraction which is related to the index of refraction by

$$\eta' = \eta + f\frac{d\eta}{df}. \tag{16a}$$

From (13b),

$$\eta' \approx 1 + \frac{\alpha E}{2f^2} \tag{16b}$$

The refractivity is therefore given by

$$N_{\text{ion}}(z) = 10^6 \frac{\alpha E(z)}{2f^2} = \frac{40.3\times 10^{12}}{f^2} E(z). \tag{17}$$

The range correction for refraction from ionospheric electrons then becomes

$$\Delta h_{\text{ion}} = 10^{-6}\int_0^h N_{\text{ion}}(z)dz = \frac{40.3\times 106}{f^2}\int_0^h E(z)dz, \tag{18}$$

where the total vertically integrated electron density is in cm^{-2}. Most of the free electrons that interfere with the propagation of electromagnetic radiation are in the region of the upper atmosphere ranging from 50 to 2000 km, with the highest concentration near 300 km (Rush, 1986). Ionization of this region of the atmosphere is attributed mostly to ultraviolet radiation from the sun. The concentration of free electrons therefore varies diurnally (by as much as an order of magnitude), latitudinally (by about a factor of 2), and seasonally (Davies, 1980; Callahan, 1984). There is also a dependence on the 11-year sun spot cycle, which will experience a maximum in solar activity in the early 1990s during the ERS-1 and TOPEX/POSEIDON missions. Typical vertically integrated electron densities range from about 10^{12} to 10^{14} cm^{-2} (Soicher, 1986; Davies *et al*., 1977). For a transmitted frequency of 13.6 GHz, this corresponds to a range correction of about 0.2 to 20 cm.

From (18), all that is required to determine the ionospheric range correction is knowledge of the vertically integrated electron density at each altimeter measurement

location. In the past, this ionospheric electron content has been obtained globally from model estimates based on twice-daily direct measurements at two locations: one in the western United States and the other in eastern Australia (Lorell *et al*., 1982). The uncertainty of these model estimates is not known quantitatively but is estimated to be 3–5 cm (Lorell *et al*., 1982). Since the range correction varies with frequency of the transmitted signal, radar altimeter measurements at two frequencies can be used to estimate simultaneously the ionospheric range correction and the vertically integrated electron density (TOPEX Science Working Group, 1981). The dual frequency TOPEX altimeter with C-band (5.3 GHz) and K_u band (13.6 GHz) transmitters will be the first to determine the ionospheric range delay directly. Errors in this range correction introduced by uncertainty in the dual-frequency estimates of ionospheric electron density are expected to have an rms value of less than 1 cm (Callahan, personal communication).

2.4 On-board Determination of 2-way Travel Time

In addition to atmospheric refraction, there are other factors which make it difficult to estimate accurately the range from the satellite to the sea surface. The reflected pulse is distorted by the presence of waves on the sea surface which complicates determination of the 2-way travel time of the pulse. Altimeter measurements of 2-way travel time are obtained by pulse-limited altimetry, which is based on a short transmitted pulse with relatively broad beamwidth (typically 1–2•). The advantage of a wide antenna beamwidth is that the 2-way travel time of a pulse is relatively insensitive to antenna pointing angle (as long as the pointing angle relative to satellite nadir is less than half the total antenna beamwidth). This is because the transmitted pulse expands spherically as it propagates so that the travel time for a short pulse to reach satellite nadir is independent of pointing angle (Fig. 2). There are, however, corrections that must be applied for off-nadir pointing angle (see Sec. 2.5.3) to account for the combined effects of antenna gain pattern and the pulse compression method (see discussion below) used to estimate the 2-way travel time of the pulse.

In the usual description of pulse-limited altimetry, the transmitted pulse has a duration of a few ns and the power of the pulse reflected from the sea surface is measured as a function of time at intervals of a few ns. The return from nadir mean sea level can be uniquely associated with a particular point in the time history of returned power. The 2-way travel time (equivalent to the range *h* after correcting for atmospheric refraction as discussed in Sec. 2.3) from the satellite to nadir mean sea level is determined by tracking

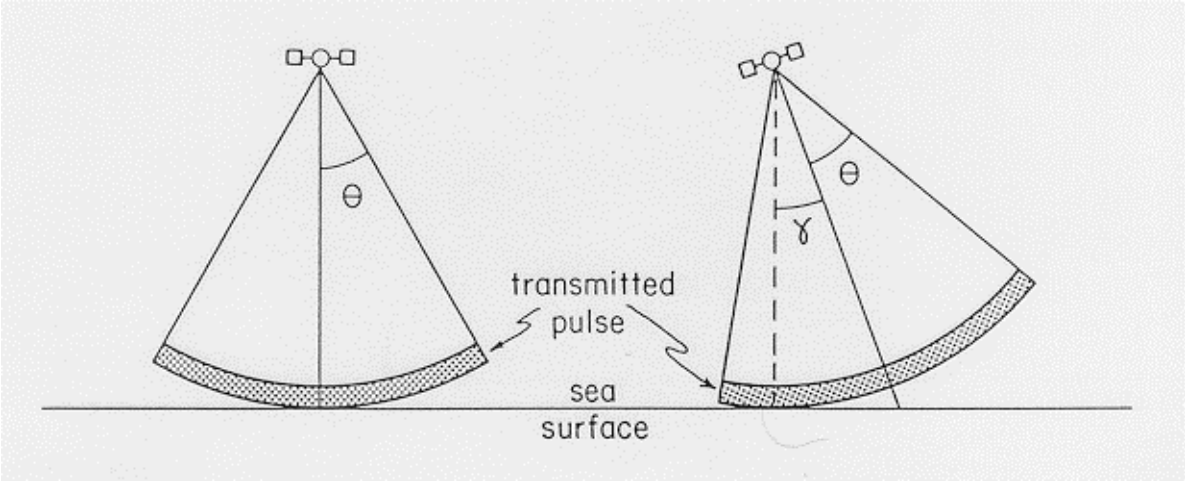

Figure 2. Schematic representation of pulse-limited altimetry with a broad antenna half-beamwidth angle θ for the case of zero pointing error (left) and an off-nadir pointing angle of γ (right). The shaded region represents the transmitted pulse.

of this point on the return waveform. Though it is convenient to think conceptually of radar altimetry in these terms, the actual technique used is quite different. The altimeter transmits a relatively long duration pulse (order μs or ms) and analyzes the returned signal in a way that is effectively equivalent to transmitting a short pulse of a few ns duration. The longer pulse length improves the signal-to-noise ratio of the measurements. The GEOS-3 altimeter used an actual pulse compression technique to expand a short pulse for transmit and compress it on receive using dispersive filters implemented in acoustic wave devices. SEASAT and subsequent altimeters use a very different technique of extracting equivalent information from a long transmitted pulse. The technique is also referred to as "pulse compression", although the term is a misnomer since a short duration pulse never actually exists at any stage in the receiver. The technique is discussed in detail in Chelton et al. (1988) and only a brief summary is given here.

The long transmitted pulse consists of a chirp with linear frequency change •F over the pulse duration τ (Fig. 3). The total signal returned from the sea surface (consisting of the superposition of the chirps returned from all specular reflectors in the antenna footprint) is then differenced with a "deramping chirp" that is identical to the transmitted chirp except that the frequency is lower by an "intermediate frequency" difference of f_{IF}. The power spectrum of this differenced IF signal is referred to as the return spectral waveform. There is a direct correspondence between frequency in the return spectral waveform and 2-way travel time for the pulse reflections from points on the sea surface in the altimeter footprint. It is shown in Chelton et al. (1988) that frequency is linearly related to 2-way travel time by

$$\Delta f = Q\Delta t\,, \tag{19}$$

where $\bullet f$ is the frequency difference relative to the frequency of the signal reflected from nadir mean sea level, $\bullet t$ is the time difference relative to the 2-way travel time for the pulse reflected from nadir mean sea level, and $Q = \bullet F / \tau$ is the frequency sweep rate of the chirp. The frequency range $\bullet F$ was 320 MHz for SEASAT and is the same for GEOSAT and TOPEX. The pulse duration τ was 3.2 μs for SEASAT and is 102.4 μs for GEOSAT and TOPEX. In addition to improving the signal-to-noise ratio, the factor of 32 increase in pulse duration reduces the transmit power requirements.

A schematic representation of the power spectrum of the return waveform is shown in Fig. 4. The power spectrum is determined on board the satellite by discrete Fourier transforms of the return signal measured in the time domain. The frequency resolution of the spectrum computed from the pulse duration τ is $\delta f = 1/\tau$. Discrete samples of the return spectral waveform at this frequency interval (referred to as "range gates", since frequency and 2-way travel time are equivalent according to (19)) are shown schematically by the heavy dots in Fig. 4. From (19), this frequency resolution corresponds to a 2-way travel time resolution of $\delta t = \delta f / Q = 1/\bullet F$, which is dependent only on the frequency range $\bullet F$ of the transmitted chirp. Since SEASAT, GEOSAT, and TOPEX all use the same frequency range $\bullet F$ = 320 MHz, the effective 2-way travel time resolution in the return waveform is 3.125 ns for all three altimeters. This corresponds to a 1-way range resolution of about 48 cm in a particular waveform. The power spectrum of the IF signal obtained from a long transmitted pulse by the deramping technique is thus analogous to the time series of returned power that would be obtained from a short pulse of 3.125 ns duration. The only difference is that the independent variable for the return spectral waveform (the abscissa in Fig. 4) is frequency rather than time. Since 2-way travel time and frequency are directly related by (19), the two representations are equivalent.

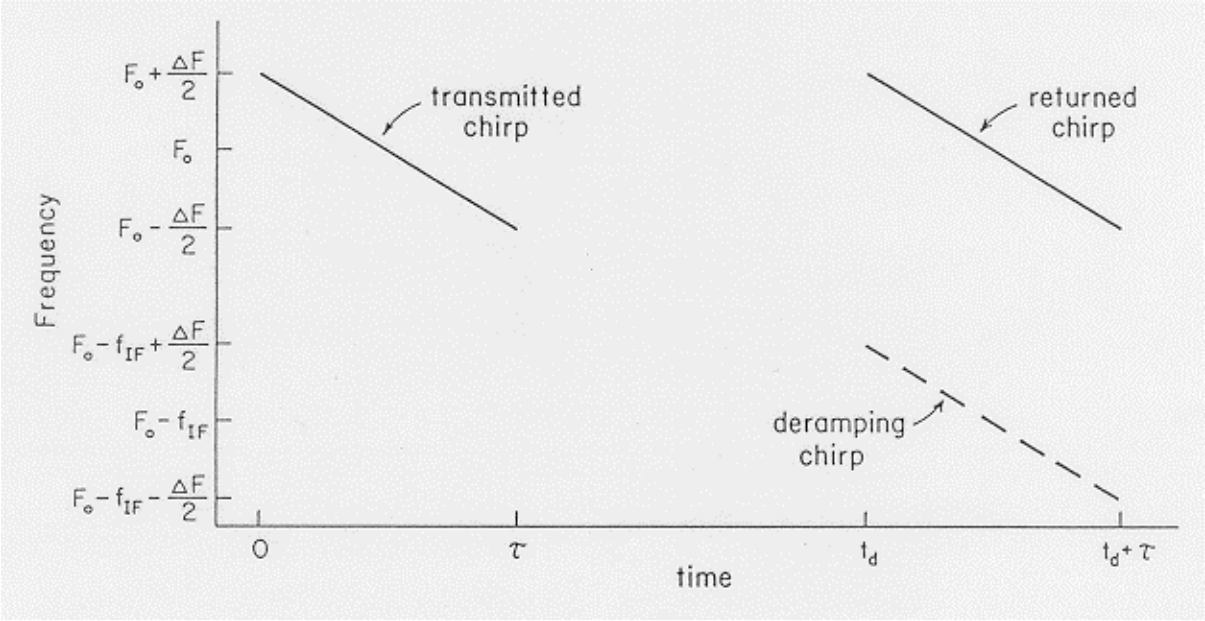

Figure 3. Schematic representation of a chirp transmitted by a satellite altimeter at time $t = 0$. The chirp frequency centered on frequency F_0 decreases linearly by amount $\bullet F$ over a sweep period τ. Also shown is the returned chirp from a specular reflector at nadir mean sea level. The returned chirps from other specular reflectors in the antenna footprint (e.g., from other points on the sea surface height distribution and from points in the antenna beamwidth away from satellite nadir) are not shown. These chirps have frequencies that differ from that of the return from nadir mean sea level by an amount proportional to the 2-way travel time as described by (19). A deramping chirp (dashed line) is generated internally by the altimeter at time t_d, which is intended to match the two-way travel time of the transmitted chirp reflected from mean sea level at satellite nadir. The deramping chirp is identical to the transmitted chirp, but with frequency lower by amount f_{IF}.

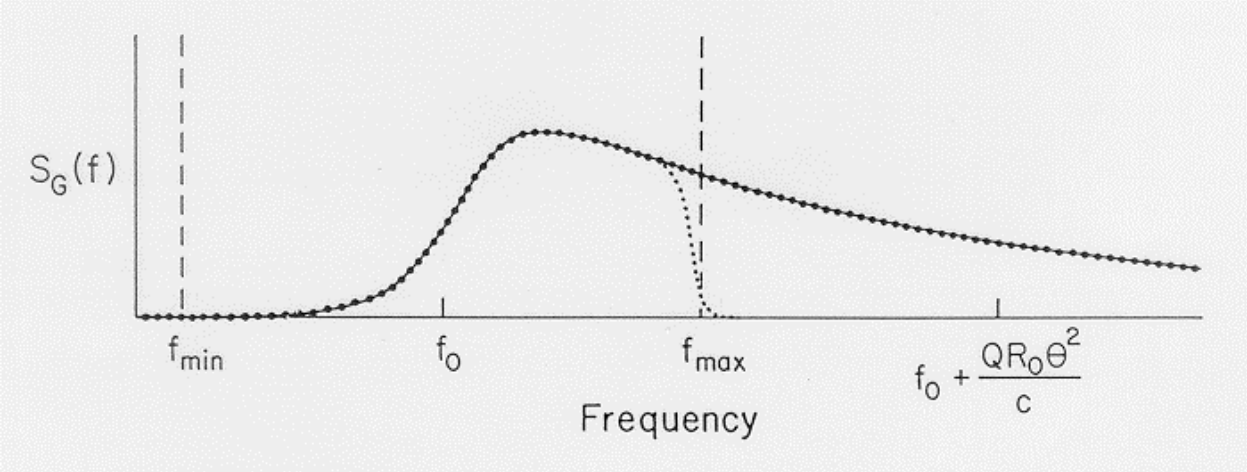

Figure 4. Schematic representation of a discretely sampled return spectral waveform (with samples shown by dots). The frequency f_0 corresponds to the return from nadir mean sea level. Only the portion of the waveform between frequencies *fmin* and *fmaz* (bracketed by the vertical dashed lines) is required for waveform processing to estimate range and significant wave height. The dotted line shows the return waveform obtained by low-pass filtering the analog received signal to remove frequencies higher than *fmaz*.

Note that although the range resolution in the discrete samples of the waveform is only about 48 cm, a much finer range precision of 0.7 cm is achieved by the altimeter. Waveform misalignment is determined from recently transmitted and received pulses as described later in this section, and the timing of the deramping chirps for subsequent pulses is adjusted with a very fine timing resolution of 0.0488 ns to shift the waveform into proper alignment. This timing resolution corresponds to a range precision of approximately 0.7 cm.

The spectrum of the total IF signal returned from the sea surface is given mathematically by a convolution of the spectrum of surface spectral reflectors *P(f)* with the antenna gain *G(f)* and the data window *W(f)* (referred to as the "point target response"),

$$S(f) = P(f) * G(f) * W(f) = W(f) * \int_{f_0}^{\infty} P(f-u)G(u)du \qquad (20)$$

(Chelton *et al*., 1988), where f_0 *is* the frequency of the signal returned from nadir mean sea level. The point target response *W(f) is* given approximately by $[\tau \sin(\pi f\tau)/(\pi f\tau)]^2$ (though in practice it is not this symmetric, see Rodriguez, 1988), and accounts for the effects of the finite record length τ from which the power spectrum is computed. The convolution with this point target response limits the frequency resolution in the return spectral waveform to $\delta f = 1/\tau$ as described above. The distribution of 2-way travel times from the satellite to the surface spectral reflectors in a small region within the antenna footprint has approximately the same shape as the sea surface height probability distribution, which is Gaussian to first order. Then since frequency and 2-way travel time are related by (19), the spectrum *P(f)* of surface spectral reflectors is approximately Gaussian, centered on frequency f_0 corresponding to the frequency of the signal returned from nadir mean sea level. It is shown in Chelton *et al.* (1988) that 2-way travel time from the satellite to the sea surface at angle θ relative to the antenna boresight increases quadratically with angle θ. From the equivalence (19) of 2-way travel time and frequency, the antenna gain as a function of angle θ can therefore be expressed equivalently in terms of frequency as *G(f)* for use in the convolution equation (20). For a typical antenna pattern, *G(f)* decays approximately exponentially with increasing frequency (Chelton *et al*., 1988). This results in an exponentially decreasing "plateau droop" at high frequencies in the return spectral waveform (Fig. 4).

An intuitive description of the shape of the return waveform can be given by analogy with the equivalent short pulse description of the waveform in terms of the power of the signal returned as a function of time from the sea surface. From the radar equation (Skolnik, 1970; Stewart, 1985), the signal power is proportional to the area on the sea surface illuminated by the antenna footprint. The footprint area as a function of time is shown in Fig. 5. After the leading edge of the transmitted pulse strikes the wave crests at satellite nadir, the footprint becomes an expanding circle. The area of the circular footprint is shown in Chelton *et al.* (1988) to increase linearly with time until the trailing edge of the pulse reaches the wave troughs at satellite nadir. Thereafter, the footprint becomes an annulus with constant area. Since the footprint outer diameter expands with time, the beam angle of the received signal increases with time. The antenna gain decreases with increasing beam angle. Thus, the power as a function of time resembles the area illuminated as a function of time, except scaled by the antenna gain pattern. This results in the "plateau droop" as shown in Fig. 4.

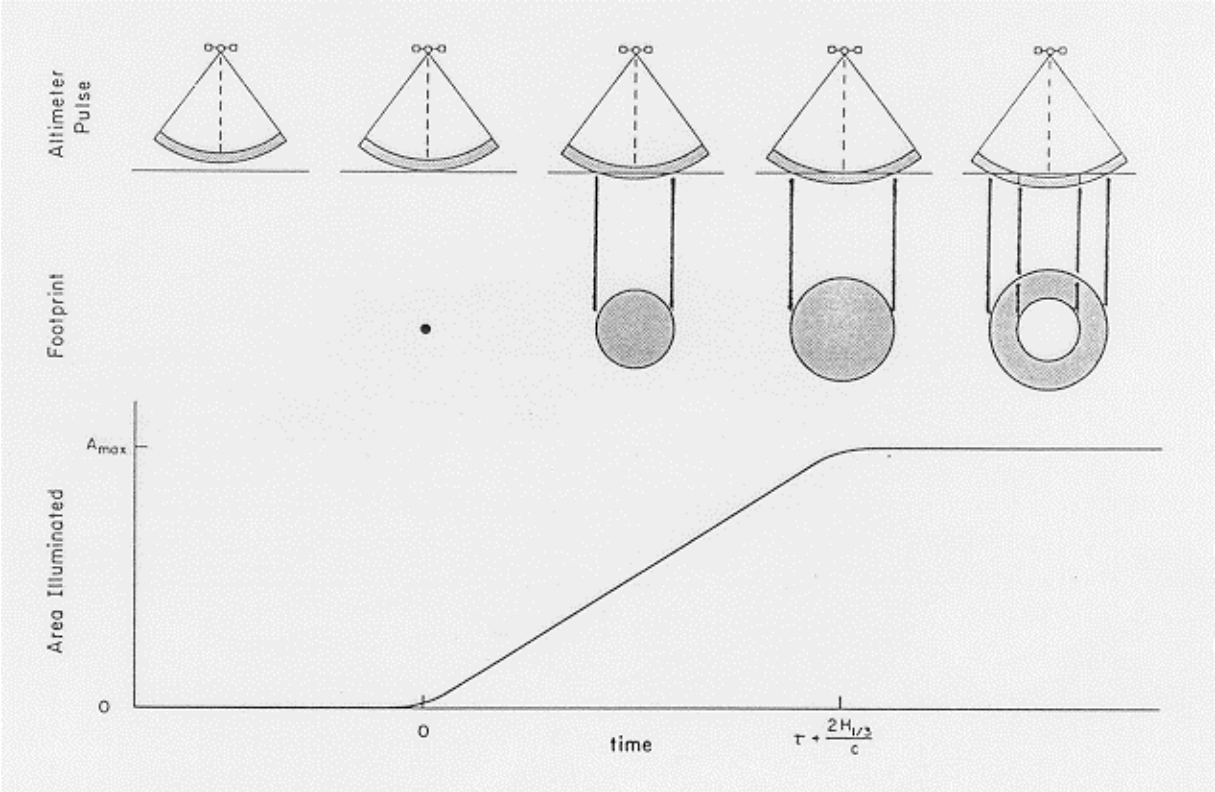

Figure 5. Schematic representation of a wide beamwidth, short pulse propagating from the satellite to the sea surface (upper row). The antenna footprint on the sea surface is shown as a function of time in the middle row. The area of the footprint is shown as a function of time in the bottom panel. For a calm sea surface, the area rise time is equal to the pulse duration τ. For a rough sea surface with significant wave height $H_{1/3}$, this rise time increases by amount $2c^{-1} H_{1/3}$.

Note that the rise time of the leading edge of the time history of the return power depends on the wave height. As wave height increases, the leading edge becomes more stretched due to the spread of the returns from wave crests and wave troughs at satellite nadir. The significant wave height (defined as four times the standard deviation of the sea surface elevation) at satellite nadir is proportional to the rise time of the leading edge of the waveform (Fig. 6). Thus, significant wave height can be estimated from the slope of the leading edge of the waveform (Walsh, 1979).

Given the probability distribution of the sea surface elevation, the pulse reflected from nadir mean sea level can be associated with a particular frequency in the power spectrum of the returned waveform. It is shown in Chelton *et al*. (1988) that, for a Gaussian sea surface height distribution, this frequency corresponds to the half-power point on the leading edge of the waveform (see Fig. 4). The altimeter adaptive tracking unit shifts the waveform in frequency to maintain the half-power point at a specified frequency f_0 (set by the time lag between the transmitted chirp and the deramping chirp). With the electronics incorporated in the SEASAT, GEOSAT, and TOPEX altimeters, this

frequency shift can be applied with a resolution of $(64\tau)^{-1}$, corresponding to a 2-way travel time resolution of 0.0488 ns and a range precision of about 0.7 cm. Frequency shifts are achieved by adjusting the timing of the deramping chirp. For proper tracking, the time lag between the transmitted and deramping chirps is equal to the 2-way travel time from the altimeter to mean sea level at satellite nadir. The speed of light used to transform from 2-way travel time to range *h* must account for the effects of atmospheric refraction from water vapor and dry gases in the troposphere, and ionospheric free electrons as discussed in Sec. 2.3.

The two geophysical quantities to be extracted from the return spectral waveform are thus the range to nadir mean sea level (which should be located at the half power point of the leading edge of the waveform if the tracker is performing properly), and the significant wave height (inversely proportional to the slope of the leading edge of the waveform). The important portion of the return waveform near the leading edge is bracketed by the dashed lines in Fig. 4. Since not all of the waveform is needed for waveform processing, the return signal is low-pass filtered to eliminate frequencies higher than some pre-determined f_{max}, as shown by the dotted line in Fig. 4. In addition to eliminating most of the unused trailing edge of the waveform, this low pass filter eliminates aliasing and allows a large sample interval in the time domain (order μs) while still retaining the full frequency resolution $\delta f = 1/\tau$ in the frequency domain (corresponding to the 2-way travel time resolution of 3.125 ns) in the discrete samples of the waveform. This filter is generally referred to as an anti-aliasing filter.

It should be pointed out that the smooth return waveform in Fig. 4 exists only in the average of many individual waveforms. Within the altimeter antenna footprint on the sea surface, there will always be many wave facets specularly reflecting the incident signal at a given range. The amplitude of the total returned signal can therefore be shown to be approximately Rayleigh distributed (Ulaby *et al.*, 1988) and the returned power (proportional to the square of the amplitude) in each range gate is therefore approximately an exponentially-distributed random variable. Since each range gate samples a different collection of wave facets, this geophysical variability results in a noise-like appearance of each individual return waveform. As the altimeter moves along the satellite orbit, the path lengths to the various facets change. The wave facet phase relationships therefore change and the return signal amplitude undergoes different Rayleigh fluctuations in each waveform. Many individual waveforms must therefore be averaged to obtain a mean waveform with the smooth shape shown in Fig. 4. If each waveform is statistically independent (which depends on the pulse repetition rate and the satellite orbital velocity, see Walsh, 1982), the Rayleigh noise decreases as the square root of the number of waveforms in the average. In practice, the tracker analyzes the average of all individual waveforms received over 1/20 s.

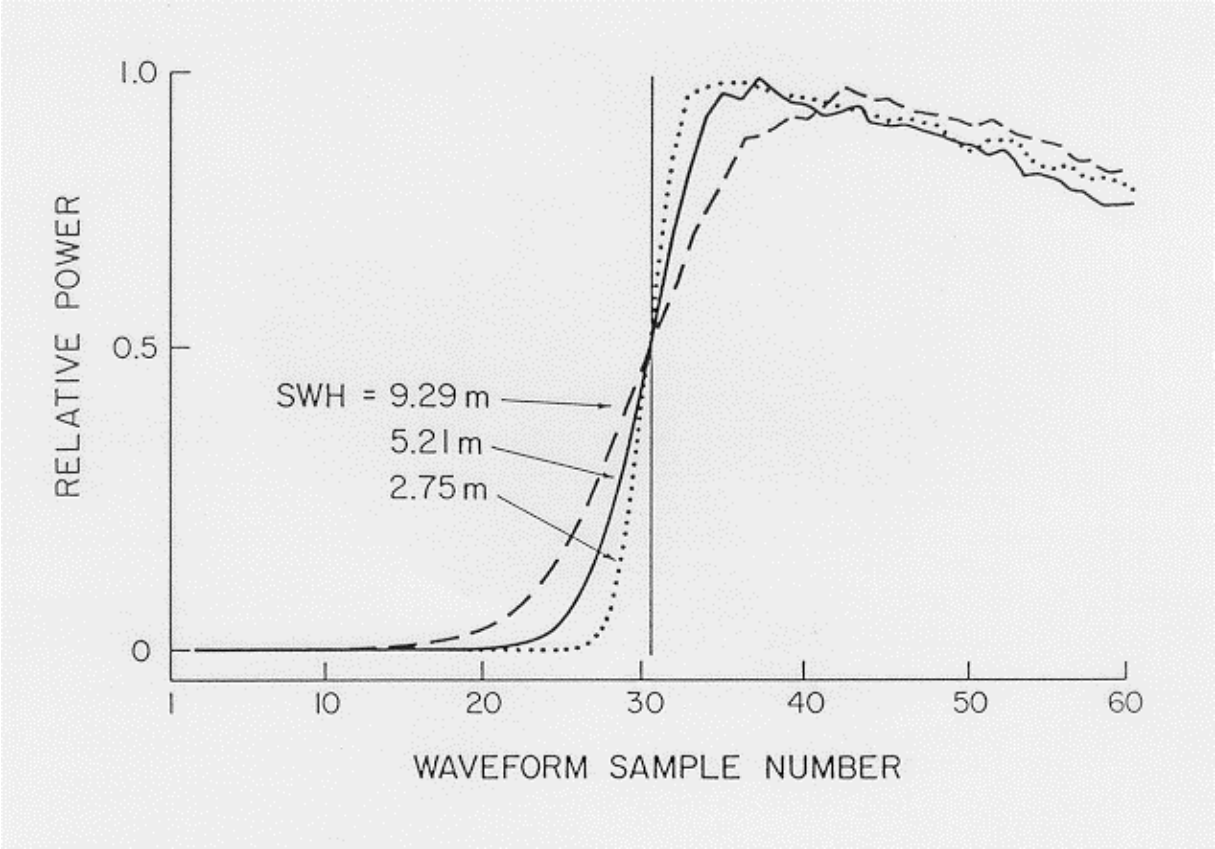

Figure 6. Example SEASAT waveforms for significant wave heights of 2.75 m, 5.21 m, and 9.29 m. The waveform sample number out of a total of 60 is shown along the bottom axis. For each waveform, the noise spectral power in the early waveform samples has been removed from each waveform sample, and the waveform samples have been scaled to have a maximum value of 1.

The tracker thus updates 20 times per second the frequency shift necessary to locate the half power point of the leading edge of the waveform at the specified frequency f_0 (Fig. 4). The tracker determines the frequency shift for proper alignment of each 1/20 s average waveform and then applies this shift to each waveform in the next 1/20 s group. This frequency shift is determined on board the satellite by computing the difference

$$D = S_{agc} - S_{mid}\,, \tag{21}$$

where S_{mid} is the spectral power in the "middle gate" at frequency f_0 of the waveform and S_{agc} is the "AGC gate" defined as

$$S_{agc} = \frac{1}{N_G} \sum_{j=1}^{N_{agc}} S_j\,. \tag{22}$$

In (22), S_j is the spectral power of the waveform at frequency f_j sampled by discrete Fourier transform. The AGC gate is thus a scaled total spectral power summed over N_{agc} (typically about 60 for past and present satellite altimeters) frequencies centered on the tracking frequency f_0. The scaling factor N_G is a fixed constant chosen so that the difference D given by (21) is zero when the waveform is properly aligned.

For noise-free waveforms, $S_{mid} = 0.5S_{max}$ (where S_{max} is the maximum spectral power in the waveform) if the half power point of the leading edge of the waveform has been placed at the middle gate frequency f_0. If the antenna gain were 1 across the full antenna beamwidth, the plateau in the waveform at high frequencies would be flat. Then the average power over N_{agc} frequencies centered on f_0 would also be $0.5S_{max}$. In this case, the scaling factor N_G in (22) would be equal to N_{agc} to make D equal to zero in (21). For a real antenna, the gain pattern and the anti-aliasing filter result in the plateau droop discussed previously (see Fig. 4), which reduces the total power summed over the N_{agc} frequencies. The power in the middle gate remains $0.5S_{max}$ for proper tracking, independent of plateau droop. The scaling factor N_G in (22) must therefore be reduced to make S_{agc} equal to $0.5S_{max}$. The appropriate value of N_G is determined pre-launch from laboratory calibration of the instrument.

As noted previously, there is residual noise in return waveforms, even in averages of a large number of individual waveforms. This noise effectively averages to zero in the 1/20 s average of the sum over a large number N_{agc} of frequencies in the AGC gate (22). The value of S_{agc} is therefore relatively insensitive to random fluctuations about the mean at each individual frequency. Residual noise can be significant, however, in the average values of S_j over 1/20 s for any particular frequency f_j. Thus, setting S_{mid} equal to the spectral value at frequency f_0 introduces noise in the value of D given by (21). In practice, noise in the value of S_{mid} is reduced by defining the middle gate to be the average of 2k spectral values centered on frequency f_0. The width of the middle gate is adjusted according to the "rise time" of the leading edge of the waveform (directly related to SWH); as wave height increases and the leading edge of the waveform becomes more stretched, the value of k is increased as a staircase function of SWH. A total of five possible middle gate selections are allowed, centered near SWH values of 1, 2, 4, 8, and 16 m. The on-board tracker is referred to as "adaptive" because of this ability to adjust the width of the middle gate according to SWH.

The value of the AGC gate is only weakly dependent on misalignment of the waveform. The value of the middle gate, however, is very sensitive to waveform alignment. If the difference D given by (21) is greater than zero, then S_{mid} is too small and the half-power point of the leading edge of the waveform was misplaced at a frequency lower than f_0. Similarly, a value of D less than zero implies that S_{mid} is too large and the half-power point was misplaced at a frequency higher than f_0. Assuming that tracking of the half power point is not off by a large amount (i.e., D is relatively small), then the tracking gate is in the vicinity of the half-power point of the leading edge where the

waveform can be approximated as a straight line (Fig. 4). Then the shift in frequency necessary to achieve $D = 0$ is

$$\Delta f' = bD, \tag{23}$$

where *b is* the reciprocal of the slope of the leading edge at the tracking gate. Since the slope of the leading edge of the waveform is inversely related to SWH, the parameter *b is* proportional to SWH. This parameter is stored in a look-up table on board the satellite as a biquadratic function (determined empirically pre-launch) of SWH and attitude angle in the five step sizes corresponding to the middle gate width used in the adaptive tracking.

The frequency adjustment (23) determined from one group of 1/20 s waveform averages is applied to all of the waveforms of the next 1/20 s cycle. Frequency shift and time lag between transmitted and deramping chirps are directly related by (19). The 2-way travel time between the satellite and nadir mean sea level for the next group of 1/20 s averages is equal to the adjusted time lag between transmitted and deramping chirps. Note that the waveforms in the 1/20 s average from which waveform misalignment is estimated are not corrected for the frequency shift (23). This is because the waveforms are sampled coarsely by discrete Fourier transforms with frequency resolution of $1/\tau$ as discussed previously. Thus, fine resolution frequency shifts given by (23) are not possible without interpolating the discretely sampled waveform. Since the frequency adjustment is updated 20 times per second, waveform misalignment is generally small.

There is still considerable residual noise-like quality in 1/20 s averages of return waveforms as a result of geophysical Rayleigh noise. This noise would lead to noise in the tracker estimate of waveform misalignment. The estimates of timing misalignment must therefore be smoothed over time to improve the estimate of frequency shift necessary to align the waveform properly with the half-power point at frequency f0. This smoothing is implemented by an "α-β tracker" which estimates the range and range rate of change since the previous tracking update cycle (Chelton *et al*., 1988). The range rate of change is due partly to an apparent range rate from noise in the individual range estimates obtained from the 1/20 s averages and partly to a true range rate from the vertical component of satellite velocity relative to the sea surface. Orbital eccentricity, oblateness of the earth, and along-track variations in sea surface topography over major topographic features in the geoid can result in a relative vertical velocity as high as 30 m/s (Born, personal communication). The timing for the deramping chirp is determined from recursion relations which smooth the preceding estimates of range and range rate with time constants α and β (see Chelton *et al*., 1988).

2.5 Instrument and Air-Sea Interface Algorithms

A number of instrumental corrections and air-sea interface corrections must be applied to obtain accurate range estimates from the on-board tracker estimates of 2-way travel time. The most important instrumental sources of error in range measurements are

the bias in on-board tractor timing estimates, calibration biases in the waveform range gate samples, the effect of antenna gain pattern on the waveform shape, errors in attenuation of the returned power applied by the automatic gain control, and antenna mispointing errors. Air-sea interface corrections include corrections for the differences between mean sea level and the median sea surface sampled electromagnetically by the altimeter (the electromagnetic and skewness biases). These are summarized schematically in Fig. 1 and are described in detail in this section (see also Chelton *et al*., 1988).

2.5.1 On-board Tracker Algorithms

As described in Sec. 2.4, the on-board tracker algorithm is designed to align the return spectral waveform so that the half-power point of the leading edge is at a specified frequency f_0. For a flat sea surface, this half-power point corresponds to mean sea level. More generally, the half-power point corresponds to the median (as opposed to the mean) of specular reflectors on the sea surface (see further discussion in Sec. 2.5.2). What is desired for the altimeter range measurement is mean sea level. When the sea surface is not flat, mean sea level and the median scattering surface differ. The difference is the sum of the electromagnetic (EM) and skewness biases discussed in Sec. 2.5.2. The on-board tracker attempts only to estimate the half-power point, without regard to its relation to mean sea level. EM and skewness bias effects are removed (to the extent possible) in subsequent ground-based processing. Sources of instrumental error in on-board tracking of the half-power point are discussed in this section.

The most obvious source of on-board tracker errors is noise in the estimates of AGC gate and middle gate values S_{agc} and S_{mid} in (21). As described in Sec. 2.4, S_{agc} is computed from 1/20 s averages of the sum of a large number N_{agc} of individual range gates in each waveform and is therefore relatively insensitive to Rayleigh fluctuations in the return waveforms. The middle gate S_{mid} is computed from a local average of $2k$ spectral values around the tracking gate. The value of k is increased as a staircase function of SWH. Because fewer individual range gates are included in the average, S_{mid} is much more sensitive than S_{agc} to Rayleigh noise. This introduces noise in the value D given by (21), which results in errors in the frequency shift $\bullet f'$ in (23) used by the tracker to correct for misalignment of the waveform. This unavoidable source of tracker noise is significantly reduced by the smoothing inherent in the α–β tractor.

A second source of tracker error is systematic errors in S_{agc}. The AGC gate given by (22) must be scaled by N_G to account for plateau droop in the waveforms. If the value of N_G used is in error because of improper modeling of the antenna gain pattern, or is not appropriate for the nominal antenna pointing angle, S_{agc} will be biased. Any residual systematic errors in the AGC gate would lead to a bias in the estimate of waveform misalignment. This error can be corrected by ground-based processing if the antenna pointing angle is known accurately (see Sec. 2.5.3).

The table look-up estimate of the parameter b (the reciprocal of the slope of the leading edge of the waveform) in the tracking shift $\bullet f^{\cdot}$ given by (23) introduces a third error in tracker performance. This staircase approximation of the waveform slope is in general not exact, thus introducing errors in waveform alignment. The look-up parameter is based on SWH, with the step size between successive look-up values increasing with SWH. Consequently, this component of tracker noise increases in magnitude with increasing wave height. This source of tracker noise could be reduced by replacing the table look-up estimate of b with an accurate estimate computed from the actual slope of the leading edge of the waveform. Note, however, that errors in b only affect the rate at which the tracker brings the waveform into proper alignment. A value of b that is too small will require several 1/20 s tracking update cycles to align the waveform properly. A value of b that is too large will result in greater tracker noise as the waveform is shifted too much in each 1/20 s update cycle. Noise introduced by the coarse resolution of b is mitigated, to some extent, by the smoothing inherent in the α–β tracker. These errors are further reduced when the range measurements are averaged over time (nominally, 1 s averages have been used for SEASAT and GEOSAT data).

The coarse look-up table resolution of the parameter b in (23) introduces an additional tracking error when the AGC attenuation is in error. For proper tracking, the value of D given by (21) is zero. In this case, D is not sensitive to the accuracy of the AGC attenuation since the same attenuation is applied to the spectral power in all range gates and the tracking gate still coincides with the half-power point. However, when the value of D is nonzero, the AGC accuracy becomes more important. Suppose the waveform attenuation is in error by a multiplicative factor C. Then the difference D is also in error by the factor C. The "rise time" of the leading edge of the waveform is independent of AGC attenuation, so the slope of the leading edge also changes by the factor C. The parameter b therefore changes by the factor $1/C$, and the frequency shift $\bullet f^{\cdot}$ of the waveform given by (23) should be insensitive to the accuracy of AGC attenuation. This is true only if the actual value of the waveform slope is used to compute b. Since b is determined from a coarse look-up table, the error in D is not necessarily compensated for exactly by a similar error in b. Errors in AGC attenuation can therefore introduce noise in the tracking of mean sea level in the waveform. This noise is similar in character to that introduced by errors in b as discussed above. These errors affect the rate at which the tracker brings the waveform into proper alignment.

2.5.2 EM and Skewness Biases

As described in Sec. 2.4, the function of the on-board tracker is to adjust the timing of the deramping chirp to maintain the half-power point of the leading edge of the returned spectral waveform at the specified frequency f_0 (see Fig. 4). This tracking is performed without consideration of the relation between the half-power point and mean sea level. There are at least two effects which result in systematic differences between the

two. If not corrected for, both of these effects tend to bias the altimeter estimate of mean sea level lower than true mean sea level.

The first bias is due to the difference between mean sea level and the mean scattering surface. The radar backscattered power per unit surface area is greater in wave troughs than near wave crests. In part, this is due to the fact that the power backscattered from a wave facet to the altimeter is proportional to the local radius of curvature for the long-wavelength (longer than a few cm) portion of the wave spectrum. Ocean waves are generally skewed such that wave troughs are flat and wave crests are peaked. Thus, the radii of the troughs are greater than the radii of crests. The result is a bias in backscattered power toward wave troughs. This bias is further enhanced by a greater small-scale roughness of the sea surface near wave crests, which scatters the altimeter pulse in directions away from the incident radiation. A possible physical explanation for the difference in roughness between troughs and crests is that the trough regions are more protected from surface winds, and hence smoother. Troughs are therefore better specular reflectors. Thus, both of these effects bias the power distribution of the reflected altimeter pulse toward wave troughs, as shown in Fig. 7. This bias is due purely to the interaction between electromagnetic (EM) radiation and the sea surface, and is therefore referred to as EM bias.

The magnitude of EM bias cannot be determined from the shape of return spectral waveform since the waveform is shifted in frequency but essentially unchanged in shape, and therefore introduces an undetectable range error (Walsh *et al*., 1988; Rodriguez, 1988). The EM bias probably depends on a variety of surface wave characteristics. The only sea state characteristic measured by the altimeter is the significant wave height (from the slope of the leading edge of the return spectral waveform). Since EM bias tends to increase with wave height, it is generally expressed as a percentage of SWH. Estimates derived empirically from in-orbit measurements range from 1–5% of SWH, but with uncertainty as large as the correction (Hayne and Hancock, 1982; Born *et al*., 1982; Douglas and Agreen, 1983).

The magnitude of the EM bias can be quite large. Significant wave heights of 10 m are not uncommon in the Southern Ocean (Chelton *et al*., 1981; Witter and Chelton, 1988). If the EM bias is 2% of SWH, this corresponds to a bias of 20 cm. If the uncertainty of the EM bias is only 1% of SWH, the resulting uncertainty in the range measurements h is 10 cm. This clearly represents a major source of uncertainty in the overall height error budget. Since SWH tends to vary latitudinally (typically 6 m in the Southern Ocean, 1–2 m in the tropics, and 3–4 m in the mid- to high-latitude northern oceans—see Chelton *et al*., 1981), any systematic errors in the EM bias would introduce latitudinal biases in the range measurements. This would result in erroneous mean zonal geostrophic currents estimated from altimeter data.

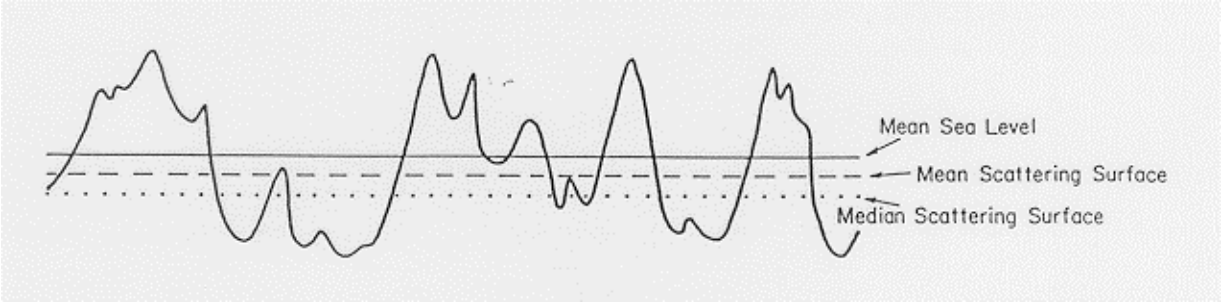

Figure 7. Schematic representation of mean sea level (thin continuous line), the mean scattering surface (dashed line), and the median of the scattering distribution (dotted line) for a rough sea surface (heavy continuous line).

Another potential source of concern for the EM bias is imprecision in the altimeter estimates of SWH. Since the EM bias is modeled as a simple percentage of SWH, noise in the SWH estimates obtained from the leading edge of the return waveforms results in noise in the bias correction. Witter and Chelton (1988) showed that the SEASAT altimeter SWH noise was about 20 cm for SWH up to 7 m, and gradually increased to about 40 cm for SWH of 15 m. For an EM bias of 2% of SWH, this corresponds to noise of only 0.4 to 0.8 cm in range estimates. This is negligible in comparison with errors due to uncertainty in the magnitude of the EM bias (i.e., uncertainty in the SWH multiplicative factor used in the EM bias correction).

The second bias is related to the non-Gaussian nature of the sea surface height distribution. Removing the EM bias discussed above, the correspondence between the half-power track point and mean sea level is exact only if the height distribution is symmetric (e.g., Gaussian). In actual fact, the height distribution is skewed (Fig. 8). Mean sea level is unchanged. However, the amplitudes of negative height deviations are reduced, and the amplitudes of positive height deviations are increased by skewness in the height distribution. The median of the height probability density function $p(h)$ corresponds to the point h_{med} where

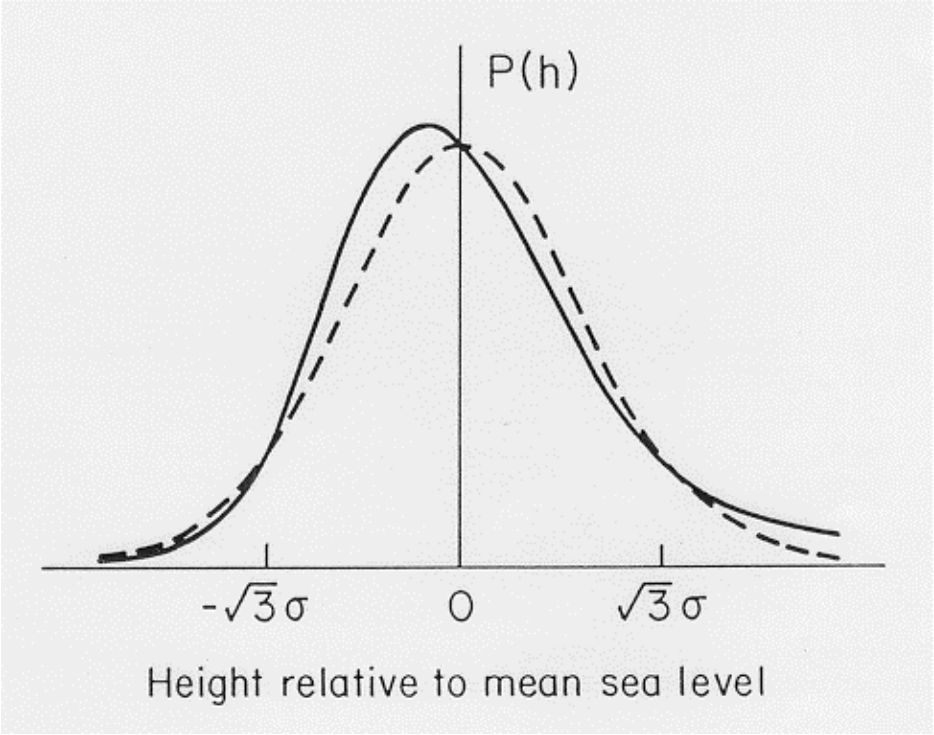

Figure 8. Comparison of Gaussian (dashed curve) and skewed Gaussian (continuous curve) sea surface height distributions relative to mean sea level. The surface height standard deviation is denoted by σ. Note that the skewed and Gaussian distributions intersect at mean sea level and ±•3 σ.

$$\int_{-\infty}^{h_{med}} p(h)dh = \int_{h_{med}}^{\infty} p(h)dh = 0.5\,. \tag{24}$$

For any symmetric distribution, the median is equal to the mean value. The median of a skewed Gaussian sea surface height distribution is shifted from mean sea level toward the wave troughs (Hayne and Hancock, 1982; Srokosz, 1986). Since the return spectral waveform described by the convolution (20) is an integral of the sea surface height probability density (weighted by the antenna gain), the half-power point on the leading edge corresponds very closely to the median of the scattering surface. Effects such as antenna pointing errors and the rolloff of the antenna gain pattern will cause the half-power point to differ from the median, but these differences are second order effects. This tracker height bias toward wave troughs due to the non-Gaussian nature of the sea surface height distribution is referred to as the skewness bias (Fig. 7).

At the present time, estimates of the magnitude of the skewness bias are very uncertain, ranging from 20% to 100% that of the EM bias (though not in any simple way related to EM bias). Correcting for the skewness bias requires knowledge of both the surface wave height standard deviation (or, equivalently, SWH) and the skewness parameter. Determination of the latter from altimeter waveforms is possible from detailed

ground-based waveform analysis (Rodriguez, 1988; Walsh *et al.*, 1988), but requires very accurate range gate calibrations (see Sec. 2.5.4). Rodriguez (1988) and Rodriguez and Chapman (1988) have estimated skewness biases of 1–4 cm from simulations and actual SEASAT data.

Clearly, further research is important to understanding better the physical basis of the EM and skewness biases and developing accurate correction algorithms. This requires a better understanding of radar scatter theory. In particular, the limitations of present approximations, the structure of the sea surface and the theory of ocean wave interactions all need to be better understood.

2.5.3 Antenna Mispointing

Off-nadir antenna pointing angles affect the accuracy of measurements of σ° and range h. The physical basis for the effects of antenna mispointing on σ° is well understood. Off-nadir pointing angles result in a loss of returned power from the combined effects of antenna gain pattern rolloff and the strong incidence angle dependence (Moore and Fung, 1979) of the coefficients A and B in the model function (1) relating σ° to wind speed. The loss in σ° can be determined accurately as a function of antenna pointing angle from pre-launch simulations and calibration of the antenna. For the SEASAT altimeter, a pointing error of 0.2° resulted in a loss of 0.4 dB in σ° (Chelton and McCabe, 1985).

The physical basis for the effects of antenna mispointing on the range estimate is also well understood. The combined effects of antenna mispointing and antenna gain pattern affect the shape of the returned waveform (MacArthur *et al.*, 1987; Rodriguez and Chapman, 1988). An example from the GEOSAT altimeter is shown in Fig. 9. Off-nadir pointing angles decrease the rolloff rate of the trailing edge of the return waveform; the plateau region is approximately horizontal when the satellite attitude angle is equal to the angle corresponding to the half-power point of the antenna gain pattern. For large pointing errors, the returned power in the plateau region can actually increase with increasing range gate because the portion of the antenna pattern with maximum gain samples a region on the sea surface far from satellite nadir. Clearly, antenna mispointing will lead to errors in the AGC gate S_{agc} given by (22) due to an overestimate of power in the plateau region. This will bias the value of S_{agc} high, which would cause the tracker to shift the half-power point of the leading edge of the waveform to a frequency higher than f_0, thus overestimating the range to nadir mean sea level (biasing the altimeter estimate of sea level below true mean sea level). Without the shape of the waveform, it is not possible to distinguish mispointing errors from frequency-shifted waveforms due to tracking errors. If not corrected, antenna mispointing of 0.2° results in a 2 cm range error for a SWH of 2 m. This range error increases approximately linearly with SWH (Rodriguez and Chapman, 1988).

Both σ• and the range *h* can be corrected for antenna mispointing, given accurate estimates of the antenna pointing angle. Historically, on-board satellite attitude sensors have not provided sufficiently accurate estimates of attitude. Furthermore, the orientation of the altimeter antenna boresight in the satellite coordinate system is known with only limited accuracy. The antenna pointing angle might therefore be estimated more accurately from the shape of the waveform in the plateau region. This method of estimating pointing angle is presently used on GEOSAT (MacArthur *et al.*, 1987), which does not carry an on-board attitude sensor. The off-nadir angle is estimated from the power summed over the last eight of 60 waveform samples (the "attitude gate", see Fig. 9). Empirical corrections based on the attitude estimate are then applied to the estimates of height and SWH. From ground simulations, the power in the attitude gate has been found to be a biquadratic function of attitude and SWH. Attitude corrections to altimeter estimates of range and AGC (and hence σ•) are linearly related to the power of the attitude gate. These corrections are applied using a table look-up formulation with coefficients that depend on SWH. The effects of imprecision in the altimeter estimates of SWH (see Sec. 2.5.2) used to search the look-up tables have not yet been investigated.

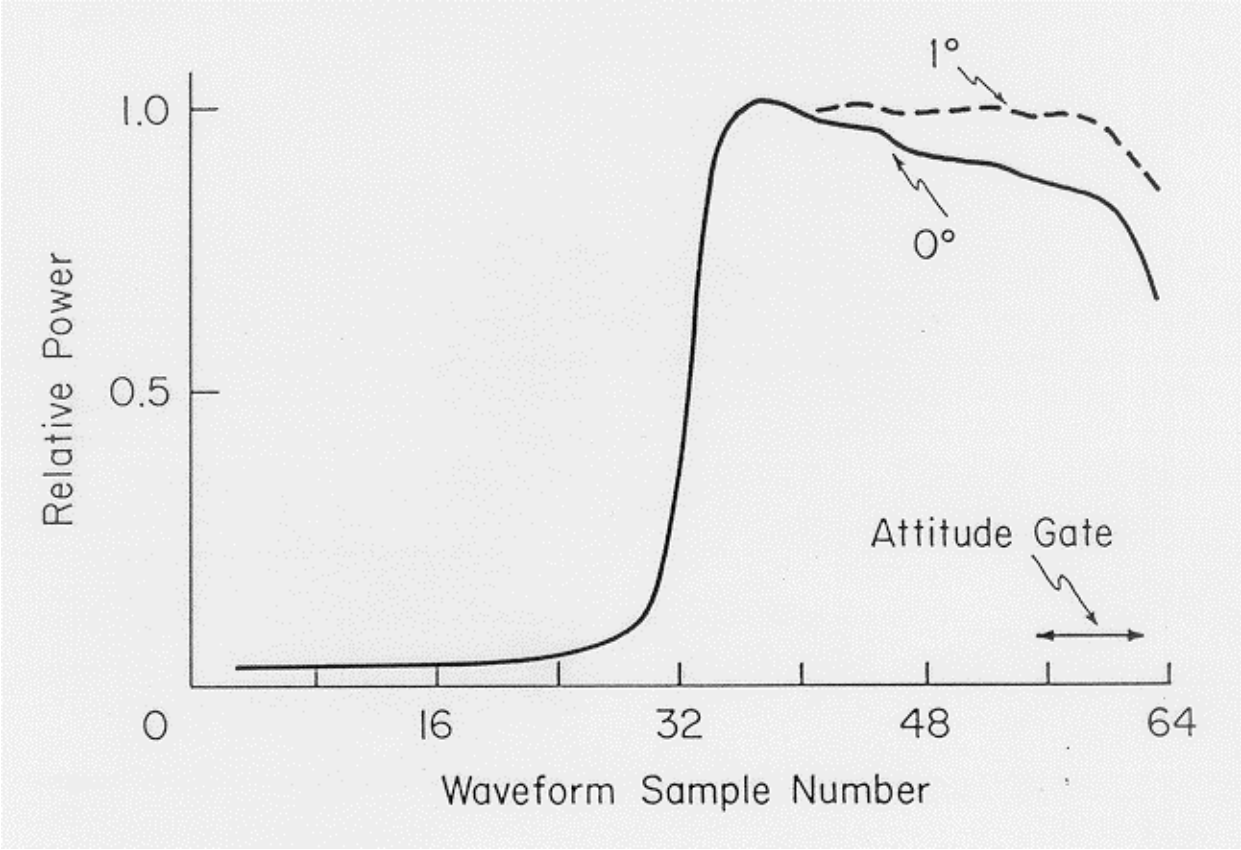

Figure 9. Example GEOSAT waveforms for 0• (solid line) and 1• (dashed line) off-nadir pointing angles. The attitude gate consisting of the spectral power summed over the last eight waveform samples is shown by the arrow.

2.5.4 Waveform Sampler Gain Calibration

Analysis of the average of many return waveforms from GEOS-3, SEASAT, and GEOSAT reveals that the power in some range gates is consistently higher or lower by small but significant amounts from that of neighboring range gates. These systematic differences are referred to as waveform sampler (or range gate) calibration errors. GEOS-3 applied a genuine pulse compression of the received signal using a dispersive delay line. The resulting short duration signal was sampled at 6.25 ns intervals by sample-and-hold circuitry. The range gate sampler calibration errors in GEOS-3 waveforms (Walsh, 1979) were evidently due to gain variations in the sample-and-hold circuits. When removed by empirical calibration corrections, the quality of the return waveforms was significantly improved.

On the SEASAT and GEOSAT altimeters, the return spectral waveforms were sampled by discrete Fourier transforms. The filter response functions were therefore exactly the same for all range gates and range gate calibration errors should in principle not exist. Nonetheless, systematic calibration differences have been found to exist between neighboring waveform samples (Hayne, 1980; Hayne and Hancock, 1987). One cause of these calibration errors is the sharp cutoff anti-aliasing filters (see Sec. 2.4 and Fig. 4) implemented on SEASAT and GEOSAT which had significant in-band ripple in the frequency response function. The TOPEX anti-aliasing filter will be designed to have lower in-band ripple, but there will still likely be small variations in the calibration of neighboring range gates. Since the characteristics of the anti-aliasing filters can be determined very accurately by laboratory calibration prior to launch, it should be easy to correct for these in-band ripple effects. Waveform sampler calibrations of this nature can also be determined post launch from the average of many noise-only measurements passed through the low-pass anti-aliasing filter.

Another suggested cause for discrete Fourier transform waveform sampler calibration errors is irregularities in the transmitted and deramping chirps (Fig. 3). The pulse compression technique described in Sec. 2.4 requires an exactly linear frequency change across the chirp sweep period. Known deviations from linear frequency sweep could be accounted for in waveform processing. These could be determined prior to launch from careful laboratory measurements. Variations in the chirp characteristics as the altimeter ages are much more difficult to determine and correct for in waveform processing. They cannot be determined from noise-only measurements. The average of many waveforms from similar sea-state conditions (so that the leading edge of the waveform is the same) must be used. It then becomes difficult to separate sampler gain variations from other geophysical variability that might have similar characteristics. The digital chirp generator used on GEOSAT and TOPEX should eliminate this second source of waveform sampler calibration errors.

For accurate estimates of range h and $\sigma\bullet$, calibration biases in waveform samples must be removed. Any residual calibration errors will result in errors in the AGC gate S_{agc}

and middle gate $S_{mid.}$ used to determine $\sigma_\bullet$ and h as described in Sec. 2.4. It is essential that methods be developed and verified for both pre-launch and post-launch determination of waveform sampler calibration biases.

2.6 External Physical Corrections

For oceanographic applications, the interest is in the sea surface elevation resulting from dynamic ocean signals. This is shown as h_d in Fig. 1. The dynamic sea surface elevation is determined from the altimeter range measurement h by

$$h_d = H - h - h_g, \tag{25}$$

where h_g and H are the geoid height and orbit height, respectively, relative to a reference ellipsoid approximation to the earth's surface. Determination of h_d from the altimeter range measurement h thus requires independent estimates of h_g and H. In addition, other external geophysical effects on the free sea surface must be removed in order to focus on signals in h_d resulting from geostrophic ocean currents. These include ocean and solid earth tides and the static effects of atmospheric pressure loading (the "inverse barometer effect"). All of these external physical corrections are discussed in this section.

2.6.1 Ocean and Solid Earth Tides

Although a thorough dynamical understanding of ocean tides is very difficult, the basic principles are straightforward. To a very close degree of approximation, tides on the earth are controlled by the moon and the sun. While other heavenly bodies contribute tidal-generating forces, their relative strengths are very small by comparison. Since the motions of the moon and the sun relative to the earth are known very precisely, it is possible to compute the tidal-generating potential to great accuracy at any point on the earth. Doodson (1922) decomposed the tidal-generating potential into 389 constituents. The total tidal-generating potential can be closely approximated by only the six constituents with the largest amplitude; these all have periods shorter than 26 hours.

If the earth were covered by a uniform layer of water, dynamical prediction of ocean tides at any location would be a simple matter since the periods, amplitudes, and phases of all tidal constituents are known precisely. However, the presence of continental boundaries and complex bottom topography in nearshore regions and the effects of the earth's rotation make purely dynamical prediction only marginally useful. In practice, ocean tides are determined empirically at selected locations. A tide gauge is installed, and measurements are made for a long enough period to resolve the principal constituents (usually a few months to a year or so). The amplitudes and phases of each of the major constituents are determined by harmonic analysis. Dynamical models of global ocean tides are then constrained by the empirically determined tidal amplitudes and phases at the tide gauges.

The amplitudes of tidal signals in the open ocean are typically 1–2 m with length scales typically longer than 1000 km (see e.g. Parlre, 1982). Tidal amplitudes are thus as large or larger than the signals of interest to altimetric studies of ocean circulation and ocean tides must therefore be removed from the altimeter range measurement h. In the past, the Schwiderski (1980a; 1980b) and Parke-Hendershott (Parke and Hendershott, 1980; Parke, 1982) ocean tide models have predominantly been used for tidal corrections. Present accuracies of these models are typically 5–10 cm globally. Errors are larger near coasts and in the southern hemisphere. This is because both tidal models are heavily constrained to coastal tide gauges, which are often not ideally located for measurement of open ocean tides and are not uniformly distributed geographically. Model inaccuracies are also large for some shelf regions and some boundary bays and seas (e.g., Patagonian shelf, Mediterranean Sea, Tasman Sea, Hudson Bay).

An important point to keep in mind is that satellite altimeter data include the geocentric tide (solid earth tide plus ocean tide), rather than only the ocean tide as observed by gauges. Therefore, both the solid earth and ocean tides must be removed from altimetric data. Solid earth tides have amplitudes of about 10–20 cm but can be modeled much more accurately (to approximately 1 cm) than ocean tides (Melchior, 1983; Harrison, 1984).

2.6.2 Atmospheric Pressure Loading

Atmospheric pressure exerts a downward force on the sea surface that is at least partially compensated for by a change in sea surface elevation. These changes in sea surface elevation are unrelated to sea surface topographic features associated with geostrophic currents and therefore must be removed to obtain the dynamic sea surface topography h_d. The hydrostatic equation for pressure p, depth z, water density ρ, and gravitational acceleration g is

$$dp / dz = \rho g . \tag{26}$$

Define $z = 0$ to be the mean free sea surface in the absence of pressure forcing. Integrating (26) from a depth z_0 to the actual sea surface height h where the atmospheric pressure is p_a, the total pressure at depth z_0 is

$$p(z_0 =) p_a + \int_{z_0}^{0} \rho g \, dz + \int_0^h \rho g \, dz . \tag{27}$$

If the ocean response to atmospheric pressure loading is isostatic (i.e., there is no net pressure change at depth associated with atmospheric pressure changes), then the first and last terms on the right hand side of (27) balance. The isostatic response is therefore

$$p_a = -\int_0^h \rho g \, dz \approx -\rho g h . \tag{28}$$

The approximation comes from the fact that ρ and g are approximately constant over the shallow depth range h near the sea surface. For atmospheric pressure p_a in mb, ρ in gm/cm^3, and g in cm/s^2, the isostatic response of the sea surface in cm is

$$h = -(\rho g)^{-1} p_a . \tag{29}$$

Using values of ρ = 1.025 gm/cm^3 and g = 980.7 cm/s^2 typical of the sea surface, this so-called "inverse barometer response" is –0.9948 cm/mb.

The change in sea surface elevation (29) to compensate for changes in atmospheric pressure results not from the compression of water but from a horizontal redistribution of water mass in response to horizontal variations in atmospheric pressure. If atmospheric pressure changed uniformly over an ocean basin, except for a negligible change due to the small compressibility of seawater, there would be no change in sea level. Thus, the sea surface response to atmospheric pressure loading depends on the spatial scale of the pressure forcing. It also depends on the time scale of the pressure forcing (Wunsch, 1972; Crepon, 1976; Brink, 1978). The transient adjustment to a change in atmospheric pressure is carried out relatively rapidly by long gravity waves. The response is believed to be nearly isostatic for time scales between about 2 days and 2 weeks (Wunsch, 1972). At shorter time scales, the ocean does not have time to compensate for the rapid pressure changes. At longer time scales, the ocean responds dynamically in the form of geostrophic currents and Rossby waves (Crepon, 1976; Brink, 1978). Ocean circulation studies require removal of the actual sea surface response to atmospheric pressure loading. The detailed wavenumber-frequency characteristics of the transfer function between sea surface elevation and atmospheric pressure loading is not known. It is likely that the transfer function varies geographically (e.g., coastal regions *vs.* open ocean regions).

The inverse barometer correction is presently a major source of error in altimetric studies of dynamic sea surface topography. The accuracy of this correction is limited by uncertainty in the actual sea surface atmospheric pressure and by uncertainty in the transfer function between sea surface elevation and atmospheric pressure loading. As noted in Sec. 2.3.1, the uncertainty in sea level pressure is probably typically about 3 mb (corresponding to an uncertainty of about 3 cm in the inverse barometer correction), but may be a factor of two or more higher in intense storms and the southern hemisphere where the sea level atmospheric pressure fields are not well resolved by meteorological models. Extreme cases of atmospheric pressure errors as large as 40 mb have been documented (Trenberth and Olson, 1988). It is clear that the inverse barometer correction can be a major source of error in altimetric estimates of dynamic sea surface topography.

2.6.3 Marine Geoid

Variations in gravitational acceleration over the earth's surface result in an uneven distribution of water mass in the oceans. There is a latitudinal variation associated with the oblateness of the earth. In addition, there are gravity anomalies associated with topographic features on the earth's surface. The gravitational acceleration at the sea surface is slightly stronger over bumps on the ocean bottom and slightly weaker over depressions in the bathymetry. In the absence of other forcing (e.g., pressure gradients, wind forcing, or tides), the sea surface would be a surface of constant gravitational potential (the marine geoid). Mathematically, the marine geoid with potential Φ_g is related to the vector gravitational acceleration **g** by

$$g = \nabla \Phi_g . \tag{30}$$

The vector gravitational acceleration is locally perpendicular to any point on an equipotential surface so that there are no lateral gravitational forces along the geoid. The vector gravitational acceleration at the sea surface in the vicinity of a bump is therefore deflected toward the bump (Fig. 10). The amount of deflection depends on the composition of the bathymetric feature and decreases as the inverse square of the distance horizontally from the bump. Thus, a bump in the far field has essentially no effect on the local gravitational acceleration. The marine geoid over a bump is therefore also a bump (though smoothed somewhat due to the inverse-square dependence on vertical and horizontal distance from the bump). Similarly, the marine geoid over a depression in the bathymetry (e.g., a trench on the ocean bottom) is also depressed. To first order then, the marine geoid is a low-pass filtered image of the bathymetry (Fig. 10).

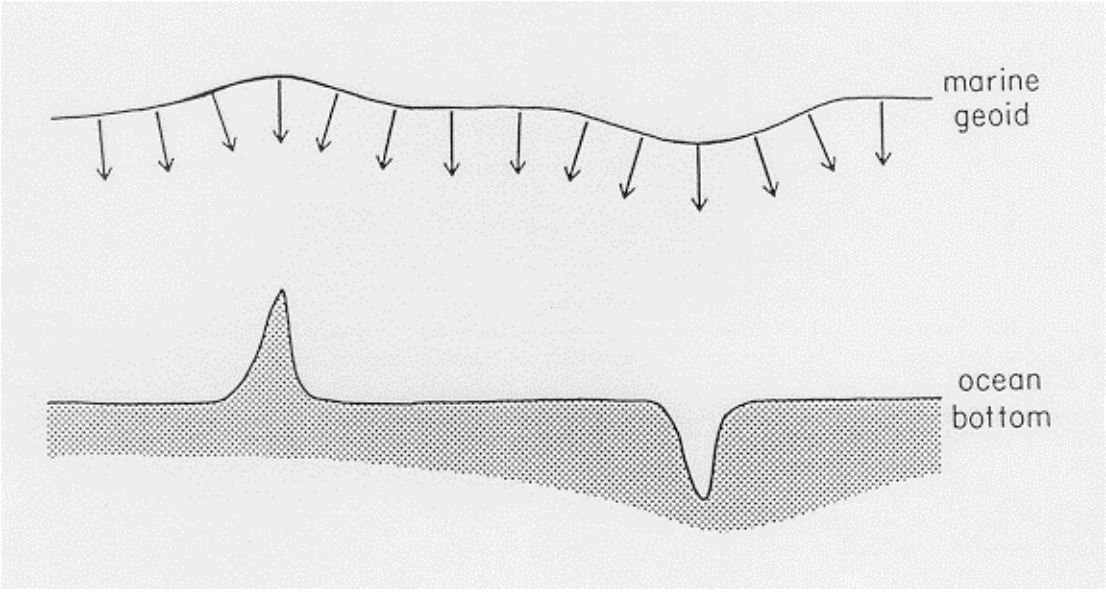

Figure 10. Schematic diagram of a bump and a depression on the ocean bottom and the corresponding marine geoid. The vectors indicate the gravitational acceleration along the geoid. The gravitational acceleration is locally deflected toward the bump and away from the depression and is tangentially perpendicular to the geoid.

Global estimates of the marine geoid are obtained from combined satellite tracking data and ship-based gravity measurements (Marsh *et al.,* 1988). The long wavelength components are obtained from measurements of the perturbed motion of near-earth satellites and short wavelength components are determined from ship-based gravity measurements. These gravity measurements are unevenly distributed globally, so there is large uncertainty of approximately 1 m in the global geoid (Marsh *et al.,* 1988). Except in limited geographical regions of densely-sampled shipboard gravity surveys (e.g., the northwest Atlantic), uncertainty in the geoid height h_g *is* the largest source of error in altimeter estimates of absolute dynamic sea surface topography h_d. Globally, the height h_g of the marine geoid (Fig. 1) has a range of about ±100 m about a reference ellipsoid approximation to the surface of the earth (Marsh *et al.,* 1988). By comparison, the sea surface topography h_d from dynamic ocean currents has a range of at most a few meters globally. Thus, to a very close approximation, the mean sea surface measured by an altimeter coincides with the marine geoid. Because the marine geoid is a low-pass filtered version of the bathymetry (as noted above), altimetric mean sea surfaces closely resemble bathymetry maps (Sloss, 1987).

Since the range of the geoid height h_g *is* nearly two orders of magnitude larger than that of sea surface topographic features h_d associated with dynamic ocean currents, the geoid must be removed for altimetric studies of ocean circulation. With geoid uncertainty of the same order of magnitude as absolute dynamic sea surface topography, it is extremely difficult to separate h_g from h_d. Problems with uncertainty in the marine geoid can be eliminated by removing the altimetric mean sea surface computed from many repeated tracks of the altimeter height measurements (e.g., Cheney and Marsh, 1981). This yields highly accurate maps of time-variable sea surface topography, but removes along with the marine geoid the component of sea surface elevation resulting from time-invariant ocean circulation. This is acceptable for studies of time-variable ocean currents, but precludes studies of absolute sea surface topography and the permanent ocean circulation. These studies require a highly accurate independent estimate of the marine geoid.

Accurate knowledge of the global marine geoid is important to altimetry for another reason. From (30), the gravitational acceleration can be computed from the marine geoid. Thus, knowledge of the marine geoid contributes to knowledge of the global gravity field. The gravity field is needed to model the satellite orbit height H (Fig. 1) between ground-based tracking measurements. Indeed, uncertainty in the gravitational field is the one of the largest sources of error in precision orbit determination (Sec. 2.6.4). Thus, improvements in the accuracy of the marine geoid will lead to improvements in precision orbit determination.

2.6.4 Precision Orbit Determination

The goal of precision orbit determination (POD) is to determine the satellite ephemeris (*H* and the latitude and longitude of the point on the sea surface at satellite nadir) and velocity relative to the center of mass of the earth. This is accomplished by statistical orbit determination using observations of the spacecraft range, range rate or angular measurements from the earth or from other spacecraft. If observations of the satellite range are available from three or more locations in a fixed coordinate system, the satellite position can be uniquely determined geometrically by triangulation. The satellite is not within the field of view of three tracking stations at all times so tracking data must be used in conjunction with a dynamical orbit model to reconstruct the satellite trajectory. The most general method of statistical orbit determination involves fitting satellite position, velocity, and selected kinematic and dynamic force model parameters to tracking data along an orbit arc by a weighted least squares procedure or by Kalman filtering (Mohan *et al.*, 1980). The advantage of these assimilation techniques over purely dynamical modeling between triangulations is that accurate estimates of the satellite position are not as sensitive to errors in the dynamical model.

There are a number of tracking systems presently in use. Microwave Doppler tracking is one of the oldest and most widely used techniques for precise orbit determination. One-way range measurements and the radial component of relative velocity between a transmitting beacon and the focal point of the receiving antenna can be determined from the difference between transmitter and receiver clock times and from the Doppler frequency shift of the received signal. Two Doppler tracking systems presently in use are TRANET (TRAnsit NETwork), originally developed in the U.S. in the early 1960s to track the U.S. Navy Transit Navigation Satellites, and DORIS (Determination of Orbit Radiopositioning Integrated from Satellite), developed more recently in France. Both systems transmit at two frequencies to enable corrections for frequency-dependent range delays due to ionospheric electrons (Sec. 2.3.3). TRANET uses frequencies of 150 and 400 MHz, and DORIS uses frequencies of 400 and 2000 MHz. The two systems differ fundamentally in basic approach. DORIS uses a receiver onboard the satellite and transmitters at about 50 ground locations, whereas TRANET uses a single transmitter onboard the satellite and receivers at about 40 ground stations. The DORIS tracking system will be used by the French for TOPEX/POSEIDON orbit determination.

The present accuracy of the radial ephemeris H estimated from Doppler tracking is approximately 50 cm for satellites such as SEASAT and GEOSAT (Marsh *et al.*, 1988, Table 23). The largest error in one-way Doppler tracking is due to timing biases between the satellite and ground station clocks. If the transmitter and receiver clocks are not perfectly synchronized, the apparent pulse travel time will be in error. This effect cannot be easily calibrated since all clocks experience some timing drifts (not necessarily simple linear functions of time). A correction for timing bias is estimated as an output of the statistical orbit determination procedure.

A new microwave tracking system called PRARE (Precision Range and Range-rate Equipment) is currently under development in West Germany (Wilmes *et al.,* 1987). The PRARE system consists of a dual-frequency two-way microwave ranging and Doppler system. The principal advantage of the PRARE system is that problems with clock calibration in the TRANET and DORIS one-way tracking systems are eliminated. The PRARE system will be used to track the ERS-1 satellite.

The TRANET tracking system will soon be replaced by GPS (the Global Positioning System). GPS consists of 18 satellites and three active spare satellites in six orbital planes with 12-hour orbits (Jorgensen, 1984). Full deployment of the GPS satellites is expected by the early 1990s. The GPS satellites continuously broadcast their geocentric coordinates and time. The 12-hour orbital period of the GPS satellites corresponds to a satellite altitude of about 2O,000 km above the earth's surface. At this high altitude, atmospheric drag and the effects of perturbations in the earth's gravity field are very small so the GPS ephemerides are known very accurately. The clocks on all GPS satellites are synchronized once per day so timing errors are also small in GPS tracking. By observing four GPS satellites simultaneously from an altimetric satellite, geocentric position and clock error relative to GPS time can be determined by solving four algebraic equations (Yunck *et al.,* 1985). Since the GPS signals generally propagate through the upper atmosphere at altitudes above the altimetric satellite (except when the GPS satellite is close to the horizon of the altimeter satellite), atmospheric refraction is generally very small. This relatively simple procedure yields accuracies of 10 to 15 m, depending on how the GPS satellites are distributed within the field of view of the altimetric satellite. This is clearly inadequate for altimetric applications. However, better than 10 cm accuracy can be attained by using simultaneous carrier phase measurements between the altimetric satellite and four GPS satellites while at the same time tracking the GPS satellites from the ground (Yunck *et al.,* 1985). This method requires accurate corrections for atmospheric refraction in estimating the ranges from the ground tracking stations to the GPS satellites. An experimental GPS receiver will be flown on the TOPEX/POSEIDON spacecraft to verify the accuracy of this tracking system.

Another tracking system important for altimetric satellites is optical laser ranging. A laser system measures the round trip travel time of an optical pulse between the ground and a reflector onboard the spacecraft. Modern laser systems have an accuracy and precision of approximately one centimeter after correcting for atmospheric refraction of the optical signal (Shawe and Adelman, 1985; Varghese *et al.,* 1988). The major limitation is that optical signals cannot penetrate clouds. As a result, laser tracking success rate is generally less than 50%. In addition, laser ranging sites are expensive to maintain so the network of ground-based lasers is relatively sparse. Consequently, while estimates of satellite ephemerides based on laser tracking are very accurate at a few points on the orbit, they can be severely degraded between laser tracking stations. The TOPEX/POSEIDON spacecraft will carry a retroreflector for laser ranging. This will be used for laser tracking and to validate the height measurements and determine the height bias residual (Sec. 6.5).

Currently, the major source of POD error is due to errors in modeling the spacecraft orbit introduced by uncertainty in the earth's gravitational field (Tapley and Born, 1980; Marsh *et al.*, 1988). Other modeling errors which degrade POD accuracy are uncertainties in spacecraft drag, solar radiation pressure, and earth radiation pressure (including uncertainty in earth albedo and atmospheric infrared transmittance). Additional errors are introduced by uncertainties in atmospheric refraction, ground station coordinates, solid earth and ocean tides, and antenna and retroreflector focal point locations. For SEASAT and GEOSAT, the orbit error was approximately 1 m in the early years after launch (Tapley and Born, 1980). Continued POD work reduced this error to less than 50 cm (Marsh *et al.*, 1988). The orbit error will be reduced even further to approximately 13 cm for TOPEX as a result of higher orbit (reduced atmospheric drag and gravitational perturbations), improved tracking, and improved orbit modeling (TOPEX Science Working Group, 1981; Marsh *et al.*, 1988).

2.7 Summary

From the summary presented in this section, it is clear that satellite altimetry is multi-disciplinary. Many instrumental and geophysical corrections must be applied to the basic altimeter range measurements to obtain accurate estimates of dynamic sea surface topography. Small errors in each of these corrections can result in a large total error. The uncertainties of several of the corrections are not presently known globally. The WOCE/NASA Altimeter Algorithm Workshop was a first step at developing a more quantitative and complete understanding of the total error budget for altimeter estimates of dynamic sea surface topography. Summaries of the workshop recommendations for the geophysical algorithms are presented in the following sections for the four categories shown schematically in Fig. 1 and listed in Table 1.

3. BACKSCATTER AND WIND SPEED ALGORITHMS

3.1 σ• Algorithm

3.1.1 Conversion from AGC to σ•

As noted in Sec. 2.2, an automatic gain control (AGC) loop is implemented in the altimeter system to assure that the altimeter electronics are operated within the linear response region of all receiver stages. The AGC analyzes waveforms averaged over 1/20 s and determines the exact attenuation that must be applied to Leep constant the output power summed over N_{agc} frequencies sampled in the waveform. This summed power is scaled by N_G to obtain the AGC gate (22) used in height tracking. The physical basis for conversion to σ• from the altimeter power measurement by the AGC is thus well understood. The particular method of low-pass filtering the return signal (see Sec. 2.4 and Fig. 4) and using only a limited number of gated samples (which do not sample the full

return waveform) rather than the total returned power to compute the AGC is questionable. An altimeter design that measures the total power return, similar to the method used by satellite scatterometers, is likely to result in more accurate estimates of σ•. The advantage is that the total returned power is independent of antenna mispointing and tracker problems associated with the gated samples method of determining σ• (Chelton and Wentz, 1986). The alternative is to insure that these effects on AGC are completely understood and correctable.

The effects of antenna mispointing (Sec. 2.5.3) on AGC and σ• are well understood. Non-zero pointing angles from satellite attitude variations reduce the power of the returned signal. The use of the slope of the trailing edge of the waveform (see Sec. 2.5.3 and Fig. 9) to estimate antenna pointing angle should be an improvement over the SEASAT processing which used a relatively low accuracy on-board attitude sensor. This method is presently used to estimate satellite attitude for GEOSAT which lacks an on-board attitude sensor.

The effects of tracker bias (Sec. 2.5.1) on AGC and σ• are not as well understood. As discussed in Sec. 2.4, the on-board tractor is designed to align the return waveform such that the half-power point on the leading edge of the waveform is located at a specified frequency f_0. If the tracker identification of the half-power point is biased low (high), then the true half-power point should be tagged in an earlier (later) range gate. The return waveforms must be shifted to correct for such tracking errors. The AGC is determined from the total power summed over N_{agc} range gates centered at frequency f_0, assuming that the half-power point is properly tracked at frequency f_0. If the waveform is aligned incorrectly due to systematic tracking errors, then the power summed over the N_{agc} range gates will be in error. It is clear then, that a bias in tracking the half-power point of the return waveform does affect the AGC (and hence σ•) value (Chelton and Wentz, 1986). Note that EM bias (Sec. 2.5.2) is the difference between mean sea level and the mean scattering surface (equal to the half-power point for proper tracking and no skewness bias). Thus, EM bias does not introduce errors in AGC or σ• since it only affects tracking of mean sea level and does not affect tracking of the half-power point.

It is important that the gain applied by the AGC loop be accurate. AGC errors result in errors in the AGC gate (29), which leads to tracker errors in estimating the misalignment (23) of the return waveform. One source of AGC error is the coarse resolution with which AGC can be applied. AGC values can only be applied in 1 dB steps with the digital step attenuators in the SEASAT, GEOSAT, and TOPEX altimeter hardware. On SEASAT, the same AGC attenuation was applied to all waveforms in each 1/20 s average, resulting in up to 0.5 dB error in the average AGC over the 1t20 s. Selective attenuation of the individual waveforms, rather than applying the same attenuation to all waveforms in the 1/20 s average will reduce the digital step attenuator source of error on future altimeters. For example, suppose that the AGC loop determines an attenuation value of 32.7 dB from a group of 50 waveforms measured over a period of

1/20 s. Then using the bank of attenuators with 1 dB step sizes, an attenuation of 33 dB is applied to the first 35 waveforms and 32 dB is applied to the last 15 waveforms of the 1/20 s average. The average attenuation over the 50 waveforms is thus 32.7 dB. This method of applying AGC attenuation has been implemented on GEOSAT with a resulting effective AGC resolution of 1/50 dB in the 1/20 s averages (Chelton *et al.,* 1988). With the larger number of transmitted pulses per second on TOPEX, the effective AGC resolution obtained by selective attenuation of the waveforms will be 1/200 dB in 1/20 s averages.

Another source of AGC error is erroneous discontinuities in the relation between AGC and σ• in ground-based table look-up algorithms. As an example, the SEASAT conversion from AGC to σ• produced discontinuous estimates of σ• because of errors in the lookup table used to implement preflight altimeter calibration data (Chelton and McCabe, 1985). **This problem could** be eliminated with a thorough analysis of the table look-up and polynomial correction algorithms developed empirically from pre-launch simulations.

Recommendations

1) *In future altimeters, calibration and conversion algorithms must be carefully examined to insure that they do not produce discontinuous geophysical parameters.*

2) *The possibility of measuring the total returned power (as is done with satellite scatterometers) rather than only a gate-limited sample of the return altimeter waveform should be explored to obtain possibly more accurate estimates of σ•.*

3) *The effects of attitude errors and tracker bias on σ• should be further investigated and correction algorithms should be developed.*

3.1.2 Absolute calibration of σ•

Wind speed has been empirically related to σ• by several different algorithms. The underlying relationship is approximately logarithmic as described by (1), with wind speed increasing with decreasing σ•. The physical basis for the relationship is not completely understood. However, the accuracy of wind speed retrievals from an altimeter is clearly directly related to σ• measurement accuracy. Absolute calibration of σ• is therefore very important.

Several proposed methods of approaching the calibration problem have been suggested. The simplest method is to form histograms of σ•. Altimeters generate many thousands of σ• estimates over the ocean each day. In a relatively short period of time, a

statistically stable estimate of the global σ• distribution can be obtained. Subtle changes in the mean σ• can therefore be detected. Month-to-month variations in mean σ• can be examined to monitor σ• calibration. Alternatively, monthly global-averaged σ• obtained from different altimeters can be compared for cross calibration. The question arises, however, as to whether detected differences are the result of calibration changes or simply natural seasonal or year-to-year variations in σ•. Some further evaluation is required to estimate the levels of natural seasonal or year-to-year variability that can be expected in σ•. This can be investigated using the multi-year GEOSAT data set.

Another potential calibration technique not yet fully explored is the use of land targets. Large regions of the Amazon rain forest and the Sahara Desert produce ocean-like radar returns. The temporal stability of such land targets is far greater than ocean targets. (Note, however, that deforestation of portions of the Amazon rain forest is a major source of concern for the stability of the radar cross section of this region.) It should therefore be possible to monitor the long-term stability of σ• measured by any particular altimeter from measurements over these regions. It might also be possible to compare the σ• measurements over land regions from different altimeters, thus allowing cross calibration of σ•. These possibilities can be explored with the existing SEASAT and GEOSAT data.

Ground-based transponders offer the prospect of absolute calibration of σ•. There are, however, several potential problems with the use of transponders. Obviously, the accuracy with which transponders themselves can be calibrated must be determined. Some transponders incorporate separate transmit and receive antennas, thus requiring a combined calibration for two antenna patterns. Since transponder measurements of σ• are certain to contain noise from a variety of sources (including imperfect corrections for 2-way atmospheric attenuation effects), any calibration program using transponders must be designed to acquire enough samples to produce a statistically reliable estimate of altimeter accuracy. This requires either a large number of transponders (increasing the problem of transponder calibration) or a long period of measurements to accumulate a large number of coincident satellite and transponder measurements. The use of transponders to calibrate σ• is also very sensitive to the beam alignment between the altimeter and the transponder. A cluster of transponders may be necessary to avoid problems with antenna mispointing, again increasing the problem of transponder calibration. Probably the greatest concern with the use of transponders is that the characteristics of the signal transmitted by the transponder may differ from those of an altimeter pulse reflected from the sea surface. Transponders might therefore calibrate the on-board tracker in a mode which it would never operate under normal conditions.

Recommendations

1) *The above methods of calibrating σ• should all be explored for future altimeters.*

2) *The multi-year GEOSAT σ• data set should be analyzed to investigate the seasonal and year-to-year geophysical stability of σ• for the calibration methods suggested above.*

3) *The problems with transponders discussed above should be investigated to determine the feasibility of this technique for calibrating σ•.*

3.1.3 Atmospheric attenuation

As discussed in Sec. 2.1, attenuation by water vapor and dry gases in the atmosphere is generally small. However, the integrated liquid water (cloud) content of the atmosphere can, on occasion, attenuate σ• by several tenths of a dB. If not corrected, this reduction in σ• would lead to overestimates of wind speed due to the form of the model function (1) relating wind speed to σ•. An error of 0.3 dB in σ• at moderate to high wind speeds results in a 1–4 m/s error in wind speed (Chelton and McCabe, 1985). The correction for atmospheric liquid water attenuation is most important in tropical regions where the cloud cover is almost always dense, or in intense storms where the integrated liquid water content can also be quite high.

Recommendations

1) *A climatological average global map of atmospheric liquid water can be determined from SEASAT and NIMBUS-7 SMMR data. This could be used to derive a simple climatological attenuation of σ• to be incorporated in the altimeter σ• algorithm. While not exact since the atmospheric liquid water can be expected to vary over a wide range of space and time scales, this climatological correction would probably be an improvement over no atmospheric attenuation correction at all.*

2) *For altimeters equipped with microwave radiometers capable of measuring the liquid water content, the inclusion of a correction for attenuation of each σ• measurement should be considered. At the very least, a data quality flag should be provided to identify suspect measurements in regions of high liquid water content.*

3.2 Wind Speed Algorithms

As discussed in Sec. 2.1, the physical basis for altimeter measurements of sea surface wind speed is relatively straightforward conceptually, though not yet completely understood theoretically. The most successful algorithms have empirically related σ• to wind speed. It is difficult to determine the accuracy of an empirical wind speed model

function tuned to any specific altimeter. This requires an extensive collection of high quality *in situ* measurements. There are two sources of error in altimeter wind speed estimates. The first is errors in the model function formulation. For example, wind speed may depend on parameters other than just σ• included in the model function. Examples include the nature of the underlying wave field (e.g., swell *vs*. wind chop) and sea surface slick contamination. Another possible factor is sea surface temperature (SST) related viscous effects on the spectral density of short waves on the sea surface. There is evidence that these effects may introduce wind speed errors in scatterometer measurements at incidence angles greater than about 10• (Liu, 1984a). At these high incidence angles, radar backscatter at about 13 GHz is from wavelengths shorter than about 2 cm. At satellite nadir (0• incidence angle), 13.5 GHz radar backscatter is from wavelengths longer than about 2 cm. The degree to which these longer waves are affected by SST-dependent viscous effects is uncertain at present.

The second source of error in altimeter wind speed estimates is measurement errors in the value of σ• used to compute wind speed. These measurement errors include imprecision in the value of σ• estimated by the altimeter hardware (Sec. 3.1.1) and errors introduced by uncorrected atmospheric attenuation of the backscattered signal (Sec. 3.1.3). Except in regions of rainfall or heavy cloud cover where the integrated liquid water content is high, these attenuation erects are generally small and are usually ignored in the estimation of σ• (Sec. 2.1). Other sources of error in σ• include errors in the correction for antenna mispointing effects (Sec. 2.5.3). As the antenna pointing angle deviates from satellite nadir, a correction must be applied to account for the fact that the radar return is not from the center of the main lobe of the antenna pattern. Uncertainty in the satellite attitude thus introduces errors in σ•.

From the general form of the relation (1) between wind speed and σ•, wind speed errors introduced by errors in the measurement of σ• increase with increasing wind speed. For example, a σ• error of 0.3 dB at 5 m/s wind speed translates to about 1 m/s error in estimated wind speed. The same σ• error at 20 m/s translates to a 4 m/s error in estimated wind speed (Chelton and McCabe, 1985). From comparisons between buoy measurements and altimeter estimates of wind speed, the uncertainty is typically 2–4 m/s in individual altimeter observations (Brown *et al.,* 1981; Dobson *et al.,* 1987). This large uncertainty is too high for many applications. Altimeter observations averaged monthly over 2• square regions reduces the error to 1–1.5 m/s (Chelton and Wentz, 1986). These monthly averages are acceptable for some applications.

Because of the difficulty in acquiring an adequate data base for empirically deriving a wind speed model function for a particular altimeter, the approach used historically has been to apply a model function developed for a previous altimeter. This should be done very cautiously. Empirical model functions are very sensitive to the absolute calibration of σ• (Sec. 3.1.2). As noted from the example above, a simple

constant bias in σ• due to calibration errors does not translate to a constant bias in wind speed, due to the inherent nonlinear nature of the relationship (1) between σ• and wind speed.

There are two possible solutions for dealing with the σ• calibration problem in wind speed estimates. The first is to mount an extensive *in situ* wind measurement program to derive an independent empirical wind speed model function for each altimeter. This approach does not require absolute calibration of σ•, but does require extensive resources and effort to acquire a large number of *in situ* wind observations over a wide range of environmental conditions. There are other problems with the use of *in situ* measurements to derive an altimeter wind speed model function (see Monaldo, 1988). As examples, vector *vs.* scalar averaging, or differences in buoy measurement averaging periods can drastically affect altimeter and buoy wind speed comparisons. The *in situ* measurement approach to model function development may not be practical for each individual altimeter mission.

The second, and possibly more promising solution to the σ• calibration problem is to cross-calibrate the σ• measurements from each altimeter. This is relatively straightforward if there is overlap between altimeter missions. However, the cross calibration is more difficult if there is no overlap of the measurement periods. Several methods are suggested in Sec. 3.1.2.

Recommendations

1) *There should be continued development of the theory of microwave backscatter at low incidence angles from a rough sea surface. Such development will likely draw attention to strengths and limitations and errors in altimeter wind speed measurements.*

2) *A technique should be developed for absolute calibration of σ• measurements so that a wind speed model function derived for one altimeter can be applied to σ• measurements from another altimeter.*

3) *For every altimeter mission, an extensive program of in situ wind speed measurements from buoys should be developed for the purpose of validating the altimeter wind speed model function.*

4. INSTRUMENT AND AIR-SEA INTERFACE ALGORITHMS

The least-understood algorithms for altimeter height measurements are the biases from instrumental on-board tracker algorithms and the air-sea interface algorithms. One of the reasons for the lack of understanding is that there is little or no physical basis for

some of these algorithms. Another problem is that documentation for some of the instrumental algorithms (including summaries of the empirical results used to derive the algorithms and rigorous error analyses) is incomplete. Strictly speaking, the instrument algorithms are not geophysical algorithms. However, they were included in the workshop discussion because of their fundamental importance to the overall height error budget.

There is considerable confusion in the terminology used to classify the various biases in the instrument and air-sea interface corrections. One commonly used convention separates the biases into "tracker bias" and "sea-state bias". In this convention, tracker bias includes all instrument-induced errors in the estimate of mean sea level obtained from the return waveform. That is, tracker bias is independent of the radar target (the sea surface). Sea-state bias then includes all other effects on the mean sea level estimate. The problem with this convention is that some of the bias effects do not conveniently fall into either category. Most notable is the distinct tracking error which increased with significant wave height on the SEASAT altimeter. As another example, antenna mispointing introduces a bias in the mean sea surface estimate that is satellite-related, but not instrument related or sea-state dependent, and therefore does not clearly fall within either category.

Another commonly used convention separates the biases into "EM bias" and "tracker bias". In this convention, EM bias includes all effects which cause the radar return power distribution (with the flat surface and point target response deconvolved, see (20)) to differ from the sea surface height distribution. Tracker bias then includes all effects in implementation of the altimeter range tracker which result in the altimeter range being different from the mean of the distribution of sea surface spectral reflectors (with the flat surface and point target responses deconvolved). This includes the bias introduced by models which do not include the effects of skewness in the sea surface height distribution nor antenna mispointing angle. It also includes instrumental biases introduced by the estimators used to produce error signals to drive the tracking loop in the instrument. An undesirable aspect of this convention is that the term tracker bias is suggestive of purely instrumental effects but this class of systematic errors also includes some biases that are clearly geophysical in nature (e.g., skewness bias).

An attempt was made at the workshop to arrive at a consensus on terminology to clear up the confusion. However, no unanimous agreement could be reached. A weak majority favored the following candidate new convention:

1) *EM bias:* Range measurement errors due to the difference between the mean surface of the ocean as sensed electromagnetically and the mean physical sea surface.

2) *Modeling bias:* At least two types of bias fall into this category:

a. *skewness bias:* Errors introduced by statistical moments of the specular point probability distribution function of higher order than variance (e.g., skewness and kurtosis). These higher order moments are not presently modeled in the on-board processing.

b. *mispointing bias:* Errors in the altimeter range measurement introduced by antenna mispointing angle. Although these effects could be removed from the data, they are not presently modeled in the on-board processing.

3) *Estimator bias:* The on-board estimator in the tracking loop used to estimate mean sea level may itself be biased due to miscalibration of the range gates or other reasons. This estimator error is purely instrumental but can vary with sea surface roughness.

Although somewhat cumbersome, the above proposed convention has the virtue of being relatively unambiguous. From the considerable discussion devoted to this topic, it is clear that the confusion about terminology will persist unless a convention is adopted and adhered to by all altimeter investigators. Given the wide range of terminology already in existence in the published literature, confusion will almost certainly persist even if a universal convention is adopted. Investigators must make clear their intended usage of terminology.

4.1 On-Board Tracker Algorithms

As described in Secs. 2.4 and 2.5.1, the on-board tracker algorithm is designed to align the return spectral waveform so that the half-power point of the leading edge is at a specified frequency f_0 (see Fig. 4). Two basic types of on-board processing of the altimeter return are, or will be, in use. The SEASAT, GEOSAT and TOPEX altimeters use the split-gate tracker summarized in Sec. 2.4. This method is based on the difference between the middle gate and the AGC gate as given by (21). The ERS-1 and POSEIDON altimeters will use a new maximum likelihood method of locating the half power point by fitting the measured waveform to a model waveform. The physical basis for both algorithms is a Brown (1977) model of the return waveform, which assumes a Gaussian distribution for the sea surface specular points (the term $P(f)$ in (20)). This assumption is a primary limitation of the on-board tracker algorithms since the actual distribution is skewed Gaussian as a result of skewness in the wave height distribution (see Sec. 2.5.2). In addition, the modeled and actual instrumental effects may differ (as was the case for the point target response of SEASAT, see Rodriguez, 1988). These effects may be corrected for in ground-based post processing, either by reanalyzing the waveform data, or by use of a table look-up correction. Since the maximum likelihood method has not yet been used operationally on any altimeter, other sources of tracking error for this method have not yet been fully investigated.

The major sources of on-board split-gate tracking errors are summarized in Sec. 2.5.1. Most of the instrumental errors are introduced by empirically-determined table look-up approximations to complete analysis of the return waveforms. Table look-up formulations and polynomial corrections for SWH and satellite attitude are used rather than complete waveform processing to reduce computation time in on-board tracking. The errors introduced by these empirically determined algorithms are among the least understood components of the total error budget for altimeter range measurements. The primary reasons for this lack of understanding are incomplete documentation of the algorithms (including error analyses) and the fact that there is little or no physical basis for some of the algorithms. A major effort must be undertaken to assure that the detailed instrumental techniques of altimetry, justifications for polynomial corrections, and error analyses of table look-up and polynomial correction procedures are thoroughly documented for all future altimeters.

Recommendations

1) *In order to intercompare data from different altimeters, the performance specifications of the different trackers must be clearly documented (including information on noise, drift, sensitivity to attitude, sea-state, etc.).*

2) *Algorithm implementation must be checked by both pre- and post-launch simulations.*

3) *The split-gate and maximum likelihood methods of on-board height tracking should be thoroughly compared through application to simulated and real (e.g. SEASAT or GEOSAT) altimeter data.*

4) *The feasibility of replacing on-board tracking algorithms with more complex ground-based waveform processing techniques for estimating range and SWH should be explored. Potentially, the waveform processing techniques may give more accurate range estimates, are less sensitive to antenna pointing errors, and provide an estimate of wave skewness. Tradeoffs between accuracy and computational efficiency of on-board vs. ground-based waveform processing techniques for estimating range should be evaluated. It is particularly important that the full potential for improving range measurements by waveform processing be evaluated for TOPEX/POSEIDON because this altimeter mission has a goal of measuring range with an unprecedented accuracy of a few cm.*

5) *Estimates for each component of instrumental error in σ°, SWH, and range determined from pre-launch simulations and calibrations should be thoroughly documented to help determine the total error budget for these geophysical quantities estimated from the altimeter data.*

4.2 EM and Skewness Biases

Biases in range measurement introduced by electromagnetic (EM) and skewness effects are discussed in Sec. 2.5.2. These two effects result in systematic differences between the half-power point of the leading edge of the return waveform and the return from nadir mean sea level. The half-power point corresponds to the return from the median of the distribution of sea surface spectral scatterers. The difference between mean sea level and the mean scattering surface is the EM bias. This is due to a greater radar cross section in wave troughs than near wave crests. The difference between the mean scattering surface and the median of the distribution of sea surface scatterers is the skewness bias. Skewness bias results from the non-Gaussian nature of the sea surface height distribution. Both EM bias and skewness bias shift the on-board tracker estimates of mean sea level toward wave troughs.

As noted in Sec. 2.5.2, the physical understanding of these two biases is very incomplete. Moreover, uncertainties in the magnitudes of these biases are as large as the estimates of the bias magnitudes themselves. EM and skewness bias are among the largest sources of error in range estimates in high sea state conditions. Especially large errors from EM and skewness bias can be expected in the Southern Ocean where SWH is always large (see Chelton *et al.*, 1981; Witter and Chelton, 1988).

Several important points regarding altimeter determination of bias should be noted. There is evidence that EM bias may vary with the transmitted altimeter signal frequency. TOPEX nighttime (to reduce frequency-dependent ionospheric range delays) measurements of height will give the differential EM bias between the two TOPEX transmitted frequencies. However, this will not be completely adequate for determining the EM bias at each frequency. In addition, EM bias will be very difficult to separate from other sources of error in altimeter signals. Effects such as errors in AGC attenuation, errors in the dry or wet tropospheric range delays (Sees. 2.3.1 and 2.3.2), errors in the inverse barometer correction (Sec. 2.6.2), the presence of patchy clouds in the antenna footprint (Goldhirsh, 1983), or errors in the Doppler shift correction of the returned signal (Chelton *et al.*, 1988) could all introduce tracking errors similar in nature to the EM bias. Additional work is necessary to determine if the EM bias can be quantified accurately and if SWH is sufficient to use in the correction. The same is true for the skewness bias.

Recommendations

1) *Quantify the magnitudes and uncertainties of the EM and skewness biases.*

2) *Further work is required to resolve whether the present algorithm for EM bias, based only on a percentage of significant wave height, is adequate. It may be advantageous to include a dependence on* σ_0 *(as an additional measure of surface roughness) in an empirical correction for EM bias.*

3) *A skewness algorithm should be developed. It remains to be determined whether or not a skewness bias correction can be made based on parameters measured by the altimeter.*

4) *The feasibility of ground-based waveform processing to estimate the skewness bias for each averaged group of waveforms telemetered to the ground should be investigated. This is especially important for the high accuracy measurements from TOPEX/POSEIDON.*

5) *Field measurements should be conducted to determine whether the EM bias is dependent on the frequency of the transmitted signal. This frequency dependence must be understood before the TOPEX dual frequency ionospheric correction (Sees. 2.3.3 arid 5.3) can be made accurately.*

4.3 Antenna Mispointing Error

The effects of antenna mispointing from satellite attitude variations are summarized in Sec. 2.5.3. Altimeter estimates of range *h* and σ• must be corrected for off-nadir antenna pointing angles. The returned power (and hence σ•) decreases rapidly with increasing off-nadir pointing angle due to the combined effects of rolloff of the antenna gain pattern and the strong incidence angle dependence of the parameters A and B in the model function (1) relating σ• to wind speed. The antenna gain pattern also changes the shape of the return waveform for off-nadir pointing angles. If not properly corrected, this change in shape leads to over-estimates of the AGC gate (22) used by the on-board tracker. This results in errors in the tracking of mean sea level as described in Secs. 2.4 and 2.5.3.

Obtaining accurate estimates of the antenna pointing angle is very difficult. Historically, the accuracy of the SEASAT on-board attitude sensor was poor. There is no attitude sensor on board GEOSAT. Even if an accurate attitude sensor existed on an altimetric satellite, the orientation of the altimeter antenna boresight in the satellite coordinate system is known with only limited accuracy. From pre-launch calibration of the GEOSAT altimeter, a new method has been developed for estimating antenna pointing angle from the shape of the return waveform (MacArthur *et al.,* 1987). This technique is based on the power of the waveform at high range gates as described in Sec. 2.5.3 (see also Fig. 9). Empirically determined corrections as functions of attitude and SWH are applied using a table look-up formulation (Sec. 2.5.2). This approach to estimating antenna pointing angle may be more accurate than using an on-board attitude sensor. This waveform analysis estimate of pointing angle will be used on TOPEX.

It is noteworthy that antenna mispointing errors will potentially be much more serious for TOPEX than for previous altimeters. TOPEX has been designed to have

highly precise attitude control and the 13.6 GHz antenna half beamwidth will be only 0.55• (as compared with 0.8• for SEASAT, for example). While the narrower beamwidth improves the signal to noise ratio in the measurements by focusing the power of the signal incident on the sea surface, the rapid roll off of the antenna gain pattern causes σ• and the range to be much more sensitive to antenna mispointing errors. The potential of determining range from waveform processing, which is relatively insensitive to mispointing errors, is thus more important to TOPEX/POSEIDON than to other altimeter missions.

Recommendations

1) *The ground-based simulations from which the empirical corrections to account for antenna mispointing effects on σ• and range based on the attitude gate should be thoroughly documented for GEOSAT and TOPEX. This will help quantify the effects of antenna mispointing on the total error budgets for σ• and range.*

2) *The statistics of GEOSAT attitude estimates obtained from the attitude gate should be analyzed to verify that this method of estimating antenna pointing angle produces reasonable and accurate results.*

3) *After launch of TOPEX, the attitude gate estimates of pointing angle should be compared with the accurate on-board attitude sensor estimates to gain some understanding of the accuracies of the two methods.*

4) *The effects of imprecision in the altimeter estimates of SWH (see Sec. 2.5.2) used to search the look-up table should be investigated. Noise in SWH estimates will result in noise in the corrections for antenna mispointing.*

4.4 Waveform Sampler Gain Calibration

As discussed in Sec. 2.5.4, empirical analysis of return waveforms from every altimeter has revealed small but systematic calibration differences between neighboring range gates. The reasons for these waveform sampler calibration errors are not completely understood. Two probable explanations suggested in Sec. 2.5.4 are in-band ripple effects of the anti-aliasing filters used to low-pass filter the return waveforms (Fig. 4), and irregularities in the transmitted and deramping chirps (Fig. 3). There may be other causes as well. The stability of these waveform sampler calibration biases is uncertain. They may vary over the lifetime of an altimeter mission.

At present, the precision of the altimeter waveform sampler gains is very uncertain. It has yet to be demonstrated that the precision and accuracy of the calibration of the antenna and waveform sampler gains is sufficient to support the various ground-based waveform processing techniques that have been proposed. The important questions

are what are the accuracy and precision of the range gate calibrations, and what accuracy and precision does any particular waveform analysis require?

Recommendations

1) *Investigate the effect of waveform sampler gain variations on sea-state and attitude dependent corrections in the on-board tracker algorithms.*

2) *The waveform sampler calibrations determined prior to launch, along with their accuracy and precision, should be thoroughly documented. Do they vary with the physical temperatures of the various components of the altimeter?*

3) *Techniques for determining waveform sampler calibration biases after launch should be investigated and tested with simulations. Can calibration biases be isolated from other sources of noise in the return waveforms? How do post-launch and pre-launch calibrations compare?*

4) *If a reliable method is found for estimating waveform sampler biases after launch, this method should be applied to the data throughout the lifetime of the altimeter to check for drifts in calibration bias.*

5. ATMOSPHERIC CORRECTIONS

5.1 Dry Tropospheric Range Correction

The physical basis for the dry tropospheric range correction is presented in Sec. 2.3.1. As described by (7), this range delay accounts for refraction from dry gases (primarily oxygen) in the atmosphere and depends only on the sea level pressure at the altimeter measurement location. The magnitude of this correction ranges from about 225 to 235 cm. The dry tropospheric range correction algorithm is the same for all altimeters. The refractivity of dry gases is accurate to about 0.2%, which introduces negligible error in the range correction. The largest source of error is uncertainty in the sea level pressure. There are several different meteorological models that could be used as a source for the sea level pressure data. Historically, the U.S. Fleet Numerical Oceanography Center pressure analyses have been used with SEASAT and GEOSAT. Pressure fields from the European Centre for Medium Range Weather Forecasts will be used in the dry tropospheric range correction for the ERS-1 and POSEIDON altimeters. The source of pressure to be used for the TOPEX range correction has not yet been decided.

It is generally assumed that sea level pressure from meteorological models is accurate to 3 mb (see Sec. 2.3.1). It is likely that sea level pressure errors are much larger in the southern hemisphere. A pressure error of 5 mb introduces a non-negligible dry tropospheric range correction error of 1.1 cm. Meteorological models also do not resolve

accurately the intensity or location of major storms. This is a problem in both hemispheres, but is probably much worse in the southern hemisphere where storms are more intense and less well sampled by ships of opportunity. Sea level pressure errors as large as 20–30 mb are not uncommon in meteorological model analyses and errors as large as 40 mb have been documented (Trenberth and Olson, 1987). This corresponds to a range correction error of 8 cm.

Recommendations

1) *Quantify errors of meteorological model estimates of sea level atmospheric pressure by comparison with direct measurements from buoys.*

2) *Evaluate the sea level pressure accuracy from several meteorological models and determine which model is the best.*

3) *The TOPEX and POSEIDON altimeters should use the same source of sea level pressure data in the dry tropospheric range correction to maintain as much consistency as possible between the two altimeter data sets.*

4) *The method used to interpolate the gridded sea level pressure field to the time and location of the altimeter measurement should be thoroughly tested.*

5.2 Wet Tropospheric Range Correction

The physical basis for the wet tropospheric range correction is presented in Sec. 2.3.2. This range delay results from refraction from liquid water droplets (clouds) and water vapor in the atmosphere. Non-raining water droplets result in less than 1 cm range correction in all but the most extreme cases. This component of the wet tropospheric range delay is therefore generally ignored. The water vapor component cannot be neglected. As described by (l0a), the water vapor range correction depends only on the vertical integral of the ratio of water vapor density to temperature. Most of the water vapor is in the lower 2 km of the atmosphere, so an effective temperature T_{eff} can be factored out of the integral. The wet tropospheric range correction then depends only on the vertical integral of water vapor density as in (l0b). The wet tropospheric range delay is largest in tropical regions and in intense storms where the water vapor content can be very high. The magnitude of the water vapor range correction varies from about 5 to 40 cm.

There are several sources of error in the wet tropospheric range correction. The refractivity of water vapor is accurate to better than 0.5%, which introduces less than 1 cm error in the range correction. The effective temperature Teff used in (l0b) varies geographically and seasonally, so that use of a single value globally introduces errors in the range correction. Uncertainty in the value for the effective temperature probably

introduces 2–4% error in the wet tropospheric range correction. This generally amounts to less than 1 cm.

The largest source of error in the wet tropospheric range correction is uncertainty in the vertically integrated water vapor. With the exception of GEOSAT, all altimeters have had or will have an on-board microwave radiometer for measuring the vertically integrated water vapor. As noted in Sec. 2.3.2, the method used is to measure the microwave brightness temperature at two frequencies near the water vapor absorption line at 22.2 GHz (Wentz, 1982). TOPEX and POSEIDON will use 18, 21, and 37 GHz; the 21 GHz channel is redundant in the event that one fails. The water vapor can be related to the difference between the brightness temperatures at two or more frequencies. From limited case studies (summarized in Sec. 2.3.2), it has been shown that microwave estimates of vertically integrated water vapor can be accurate to 0.3 gm/cm^2, which corresponds to approximately 2 cm accuracy in the range correction. It has not yet been demonstrated that this accuracy can be achieved globally during all seasons. Errors as large as 0.5 gm/cm^2 have been documented (Grody, 1976; Staelin *et al.*, 1976).

The TOPEX microwave radiometer is identical in design to the scanning multi-channel microwave radiometer (SMMR) used on SEASAT and NIMBUS-7, except that the scanning mechanism has been eliminated so that the radiometer boresight is pointed at satellite nadir. A major concern with any passive microwave radiometer is calibration drifts and biases in the brightness temperatures. Both previous SMMRs have shown considerable calibration drifts (particularly on NIMBUS-7) (Wentz *et al.*, 1986; Francis, 1987). The derivative of the microwave brightness temperature model function (Wentz, 1982) with respect to the vertically integrated water vapor is approximately 12•K per gm/cm^2 (Wentz, personal communication). Thus, from the form (10) of the wet tropospheric range correction, a brightness temperature error of 5•K corresponds to a range error of nearly 3 cm. Brightness temperature drifts can be as large as 5–15 •K. Clearly, it is important to monitor the calibration of microwave radiometers used in the water vapor range correction.

Another source of concern is the large footprint of microwave radiometer measurements of brightness temperature. The footprint size for a frequency of 18 GHz is about 50 km for a 0.8 m antenna. However, land contamination in the antenna side lobes can render the microwave estimates of vertically integrated water vapor useless. Since microwave emission from land is much higher than from the sea surface, this side lobe contamination limits the use of microwave data to regions of the ocean more than about 150 km from land. Thus, microwave data cannot be used in the wet tropospheric range correction close to land.

In the event that the on-board microwave radiometer fails or becomes hopelessly miscalibrated, it will be necessary to use vertically integrated water vapor estimates from a meteorological model as a backup data source. Model estimates are the only source of water vapor data for GEOSAT since it does not have an on-board microwave radiometer.

The errors in meteorological model estimates of water vapor vary geographically and seasonally. Furthermore, comparisons with vertically integrated water vapor estimated from microwave radiometers have shown that the model estimates are generally biased and fail to resolve features in the water vapor field with length scales shorter than about 2000 km (Fu, personal communication). Analysis of GEOSAT data has suggested that use of model estimates of water vapor may be only marginally better than ignoring the water vapor correction altogether (Cheney, personal communication), which introduces a relatively long-wavelength uncertainty of order 10 cm in the range estimates.

Recommendations

1) *Analyze historical radiosonde measurements to determine the value of effective temperature to be used in the wet tropospheric range correction (l0b). If the data are sufficient, determine the geographical dependence of this effective temperature.*

2) *Encourage the development of an extensive microwave radiometer calibration effort to be implemented during the full lifetime of each altimeter mission to monitor calibration drifts.*

3) *Evaluate techniques for obtaining estimates of vertically integrated water vapor close to land.*

4) *Encourage meteorological centers to produce vertically integrated water vapor fields. Some models presently produce only humidity at a few discrete levels in the atmosphere. This is not sufficient to obtain accurate estimates of the total vertically integrated water vapor density by integrating over the few discrete levels output by the model.*

5) *Quantify errors in meteorological model estimates of vertically integrated water vapor by comparison with direct measurements from radiosondes at many geographical locations (ranging from tropical to high latitudes).*

6) *At frequencies near 22 GHz, the brightness temperature is dependent on water vapor and (to a lesser extent) wind speed. The possibility should be explored for using altimeter wind speed measurements to separate the wind speed effect from the microwave brightness temperatures, thereby improving the microwave estimates of vertically integrated water vapor. Such an accuracy improvement would reduce the error in the wet tropospheric range delay.*

5.3 Ionospheric Electron Range Correction

The physical basis for the ionospheric range correction is presented in Sec. 2.3.3. At the microwave frequencies of interest to altimetry, the ionospheric range correction as described by (18) is proportional to the total vertically integrated electron content between the altimeter and the sea surface. The magnitude of this correction ranges from about 0.2 to 20 cm and varies diurnally and latitudinally, and to a lesser extent, seasonally and with the solar cycle. The ionospheric range delay decreases with increasing frequency of the transmitted pulse. The TOPEX altimeter will use this frequency dependence of the ionospheric range delay to obtain direct estimates of ionospheric electron content from a dual-frequency altimeter. The ionospheric range correction determined from these direct estimates is expected to be accurate to better than 1 cm (Callahan, personal communication).

All other altimeters have used, or will use, model estimates of ionospheric electron content. Furthermore, if one of the TOPEX frequencies fails, model estimates of ionospheric electron content will have to be used as a backup for the direct measurements. The source of the model data differs for the different altimeters. Modeling of ionospheric electron content is mostly empirical and based on a very limited number of direct observations. The model-based ionospheric range corrections therefore have large uncertainty (probably 3–5 cm, Lorell *et al.,* 1982). Model uncertainty is highest during times of high solar activity as will exist during the early 1990s. Models also do not resolve short-scale features in the ionosphere. It may be possible to improve the accuracies of ionospheric models using measurements of the vertically integrated ionospheric electron density from the GPS satellites or from the TOPEX dual-frequency altimeter.

Evidence suggesting that the EM bias may be frequency dependent (Sec. 4.2) is a source of concern over the dual frequency TOPEX estimate of the ionospheric range correction. If both effects vary with frequency, it may be difficult to separate EM bias from ionospheric effects. Some understanding of the differential EM bias at the two TOPEX frequencies can be gained from analysis of nighttime TOPEX measurements when the ionospheric range delay is essentially negligible. Note, however, that only the differential bias can be determined by this method; the absolute EM bias at each frequency cannot be determined. Given the significant wave height at each altimeter measurement location (determined from the slope of the leading edge of the waveform as discussed in Sec. 2.4), this sea-state dependent differential EM bias can then be subtracted from range differences at all times of day obtained from the two transmitted frequencies, thus separating EM bias effects from ionospheric effects.

Another source of concern over the ionospheric range delay is pulse dispersion introduced by the frequency dependence of ionospheric effects. At a frequency of 13.6 GHz with a chirp frequency range $\bullet F$=320 MHz, pulse dispersion is small. However, at the lower TOPEX frequency of 5.3 GHz, pulse dispersion over the same chirp frequency range may be significant. Such pulse dispersion would alter the shape of the return spectral waveform due to differential range delay from the lowest to the highest

frequencies of the chirp frequency bandwidth •*F* (see Fig. 3). Any distortions of the waveform will result in tracking errors, which translate into errors in the range and significant wave height estimates.

Recommendations

1) *Investigate whether pulse dispersion at the 5.3 GHz TOPEX frequency from ionospheric effects will introduce significant tracking errors.*

2) *Quantify errors in the dual-frequency estimate of the ionospheric range correction.*

3) *Quantify errors in model estimates of vertically integrated ionospheric electron content.*

4) *Improve ionospheric models by comparison with direct observations from dual frequency data of various sources (e.g., from GPS measurements and the TOPEX dual frequency altimeter). DORIS microwave tracking data may also be useful, although the Doppler measurements only provide estimates of changes in ionospheric electron content and not the total electron content itself.*

5) *Evaluate errors in the method used to interpolate model estimates of ionospheric electron content to the time and location of each altimeter observation.*

6) *Determine what effect differential EM bias at the two TOPEX altimeter frequencies will have on the estimate of ionospheric electron content.*

6. EXTERNAL PHYSICAL CORRECTIONS

6.1 Ocean and Solid Earth Tides

The ocean and solid earth tide contributions to the sea surface elevation are discussed in Sec. 2.6.1. These tidal signals can be very large (typically 1–2 m for ocean tides and 10–20 cm for solid earth tides) and must be removed for studies of dynamic sea surface topography h_d. Presently, ocean tides can be modeled with 5–10 cm accuracy and solid earth tides can be modeled with about 1 cm accuracy. There was considerable discussion by this working group of improvements that could be made to present tide models. Work currently underway in both Europe and the United States using combined tide gauge measurements and altimetry could provide substantial improvements in knowledge of the tides. Much of the discussion of this working group focused on making additional tidal measurements to improve the accuracies of tidal models. As noted in Sec. 2.6.1, tide models are heavily tuned to tide gauge records. Because tide gauges are not distributed uniformly globally, there are strong geographic dependences in the accuracies

of the tide models. This makes it difficult to judge which tidal model is best for a particular region of the ocean. Without additional tide gauges, these problems are likely to become increasingly difficult as the accuracies of tidal models improve.

It should be noted that the accuracies of tidal models will be very high if the amplitudes and phases of the major tidal constituents can be determined globally from direct altimeter measurements. Clearly, measurements from a single altimeter satellite with a repeat orbit period of several days to a few weeks cannot resolve the major tidal constituents with periods on the order of a day or shorter. The tidal variability will alias into the lower frequencies that can be resolved by the altimeter measurements. The SEASAT orbital characteristics have allowed determination of the M2 tide (the tidal constituent with the largest amplitude). Mazzega (1985) solved for the M2 tide by fitting the SEASAT altimeter data to a truncated series of spherical harmonics. This solution is contaminated to some extent by errors in the orbit height *H*. Agreement between the Mazzega (1985) solution and existing knowledge of the M2 tide is good in the northern hemisphere. Agreement is worse in the southern hemisphere, probably because of larger errors in orbit height due to fewer ground-based tracking stations. Woodworth and Cartwright (1986) solved for the M2 tide by expanding SEASAT altimeter data in terms of global normal modes of the ocean derived by Platzman *et al.* (1981). Agreement with existing knowledge of the M2 tide is more uniform between the northern and southern hemispheres, but the accuracy of the solution is limited by the accuracy of the normal mode calculation.

If the altimeter satellite orbit is chosen carefully (Parke *et al.*, 1987), none of the aliased periods will coincide with known energetic narrow-band variability from other causes (e.g., the zero frequency, and the annual or semiannual periods). This has been one of the strongest constraints on the TOPEX orbit. After the global amplitudes and phases of the major tidal constituents have been determined from the TOPEX data, tidal aliasing will no longer be a major constraint on the orbits of future altimeter satellites.

Recommendations

1) *There should be a sub-group formed of the TOPEX/POSEIDON and ERS-1 Science Working Teams to investigate the above problems and make recommendations to each satellite altimeter project.*

2) *A final decision on the best tide model for correcting altimeter measurements of sea surface topography should not be made until as close as possible to the launches of TOPEX/POSEIDON and ERS-1 to allow the maximum time for improvement of present models.*

3) *Consideration should be given to the use of a combination of sources for tidal information such as regional models and global models developed with the inclusion of altimetry data or direct satellite tracking data.*

4) *Over the next few years there should be a study (perhaps by the IAPSO Commission on Mean Sea Level and Tides) to evaluate on a geographic basis the accuracies of tide solutions. The forecast ability of the tide models should be checked against direct observations.*

5) *This working group supports Resolution A by the IAPSO Commission for Mean Sea Level and Tides adopted at the IUGG/IAPSO meeting in Vancouver in 1987. This resolution notes the importance of sea level measurements to monitoring ocean circulation, flow through straits, climatic changes with decade time scales, and to calibrate satellite altimetry. It therefore recommends that maximum effort should be made by all national authorities to install new tide gauges and to maintain, renew, and calibrate old gauges at as many oceanic sites as possible (especially at sites spanning straits).*

6) *There should be more study of the importance of minor constituents and long period tides and tidal models should be augmented accordingly.*

7) *The method of interpolation of the tidal value to the time and location of each altimeter measurement location needs to be carefully examined and tested.*

6.2 Atmospheric Pressure Loading

The effects of atmospheric pressure loading of the sea surface are summarized in Sec. 2.6.2. The isostatic inverse barometer response of the sea surface to atmospheric pressure is approximately 1 cm/mb. This is presently one of the largest sources of error in altimetric estimates of dynamic sea surface topography h_d. There are two issues important to the accuracy of the inverse barometer correction. The first is uncertainty in the actual sea level atmospheric pressure; the accuracy of the correction for atmospheric pressure loading can be no better than the accuracy of the pressure data used in the correction. Since atmospheric pressure data are needed globally, meteorological model forecasts of sea level pressure must be used to correct altimeter range measurements for the inverse barometer effect.

As noted previously (Sec. 5.1), meteorological model estimates of sea level atmospheric pressure contain geographically dependent errors of unknown magnitude. It is therefore difficult to quantify the magnitude of the error introduced by uncertainty in the atmospheric pressure values. From comparisons with *in situ* measurements in the northern hemisphere, model estimates appear to be accurate to approximately 3 mb (TOPEX Science Working Group, 1981). This corresponds to approximately 3 cm

uncertainty in the inverse barometer correction of the sea surface elevation. Since ship coverage of the southern hemisphere is much less extensive than the northern hemisphere, larger errors in the inverse barometer correction can be expected in the southern hemisphere. Typical pressure errors are probably as large as 5–10 mb, corresponding to about 5–10 cm error in the inverse barometer correction. Meteorological model uncertainty is also much larger in intense storms in both hemispheres. Cases of 40 mb error have been documented (Trenberth and Olson, 1987). Intense storms are generally relatively short-lived. The ocean response to storms is therefore probably not completely isostatic, so the error introduced by uncertainty in sea level pressure is probably somewhat less than 1 cm per millibar of pressure error, but is still large in these extreme cases.

The second problem with the inverse-barometer correction is uncertainty in the wavenumber-frequency transfer function between sea surface elevation and atmospheric pressure as discussed in Sec. 2.6.2. The inverse barometer response is approximately 1 cm/mb, but the exact response depends on the space and time scales of the pressure forcing. Uncertainty in the transfer function between atmospheric pressure loading and sea surface response is also a problem with sea level measurements from tide gauges. However, time series of tide gauge data are generally low-pass filtered to retain only frequencies lower than about 1 cycle/day. This is done primarily to remove most of the tidal signals (see Sec. 2.6.1), but it also very effectively removes the signals with time scales too short for isostatic inverse barometer response. With these filtered time series, a correction of 1 cm/mb probably does not introduce large errors. By the nature of altimeter sampling characteristics, time series of sea level at a given location are sampled very intermittently at intervals of 3–20 days (depending on the repeat orbit period). It is therefore not possible to low-pass filter the altimeter data in the same way that tide gauge data are analyzed. Applying a simple 1 cm/mb correction to instantaneous altimeter range measurements can clearly introduce large errors since the ocean cannot respond isostatically to atmospheric pressure disturbances with very short time scales. On the other hand, applying no pressure correction at all is also clearly incorrect. Without accurate estimates of the wavenumber-frequency characteristics of atmospheric pressure and the transfer function between sea surface elevation and atmospheric pressure forcing, it will not be possible to apply accurate corrections for ocean response to atmospheric pressure loading.

Recommendations

1) *Numerical experiments should be conducted to study the transfer function between the ocean response and atmospheric pressure forcing as a function of geographical location and the wavenumber-frequency characteristics of the forcing. It may be feasible to run a pressure response model in near real time to determine globally the appropriate pressure correction to apply to the altimeter range measurements.*

2) *GEOSAT data should be used to study empirically the inverse barometer effect (e.g., compute the coherence between repeat track differences in pressure and sea level).*

3) *The possibility of using scatterometer winds and a planetary boundary layer model to estimate the surface geostrophic pressure gradient and determine the associated surface pressure should be explored (Brown and Levy, 1986). This will require the use of in situ pressure observations as reference values for integrating the pressure gradients.*

4) *Meteorological forecast centers should be encouraged to assimilate scatterometer winds in the models to improve the accuracies of all meteorological variables (including sea level atmospheric pressure) output by the models. ERS-1 scatterometer winds will be assimilated in real time into the European Centre for Medium Range Weather Forecasts model. Winds from the NASA scatterometer (NSCAT) will not be available in real time. Any assimilation of NSCAT winds will therefore have to be done in reanalyses of the meteorological fields. Since reanalysis is not normally the responsibility of meteorological centers, significant research funds would likely be required to perform these model reanalyses.*

5) *A systematic evaluation of the various operationally produced atmospheric pressure fields should be performed. This will yield some understanding of the magnitude of uncertainty in model estimates of sea level atmospheric pressure.*

6) *Pressure gauges should be placed on WOCE drifting buoys, especially those in the southern hemisphere, to improve the accuracy of meteorological model forecasts of sea level pressure.*

6.3 Marine Geoid

As discussed in Sec. 2.6.3, in the absence of other forces, the sea surface would coincide with the marine geoid. Globally, the marine geoid has a range that is about two orders of magnitude larger than the dynamic sea surface topography associated with ocean currents. It is therefore necessary to remove the marine geoid from the altimeter range measurements for altimetric studies of absolute dynamic sea surface topography. However, uncertainty in the marine geoid is presently as large or larger than the amplitude of the topographic features associated with ocean currents. Until a more accurate global marine geoid is available, except for studies of the long-wavelength permanent circulation, most altimetric studies of ocean circulation will be limited to time variable sea surface topography obtained by removing a global mean sea surface.

A dedicated effort is underway in both Europe and the U.S. to produce an improved global marine geoid. There are basically two types of global geoids: those

based exclusively on satellite tracking and those with long wavelength components based on satellite tracking and short wavelength components based on surface gravity data and/or altimeter data. The satellite-only models are highly accurate at long length scales (about 7500 km and longer), but lack detail at shorter wavelengths. The combined gravity models have enhanced short scale detail but also include the time-invariant ocean circulation signal due to the inclusion of altimeter data. In some regions there are accurate high resolution regional geoids developed from detailed ship-based gravity surveys. These regional geoids may be of great value to ocean modelers. It might be useful to consider including estimates of geoid height from several geoid models on altimeter geophysical data records.

The only unambiguous knowledge of the global gravitational field comes from the study of the perturbed motion of near-earth satellites and is therefore a highly truncated series of spherical harmonics. However, an altimetric mean sea surface allows an approximation of the global geoid to much higher degree and order than can presently be obtained from the global distribution of surface gravity measurements alone. The disadvantage is that the altimetric mean sea surface includes both the geoid and the time-invariant component of geostrophic ocean currents as discussed previously. A decision must be made as to which description of the geoid is most suitable—one which is more complete but biased by oceanographic processes, or one which is less complete and less accurate at short wavelength, but directly based on the external gravitational attraction of the earth. It should be noted that geoidal uncertainty is non-uniform globally with either description. It varies strongly as a function of wavelength and somewhat less as a function of geographical location. Quantitative estimates of these errors would be extremely useful.

Another issue that must be considered is temporal variations in the global geoid, especially those which are not normally considered to be tidal in nature. Examples include seasonal mass changes associated with snow cover and ground water. Although small, some of these temporal variations may be important in determining satellite orbits.

Recommendations

1) *Consult with the oceanographic community as to which type of geoid model is most suitable for oceanographic studies from altimeter data: a model based solely on satellite tracking, or one based on combined satellite tracking, in situ gravity measurements, and altimetric data. Perhaps both types of geoids should be provided.*

2) *Decide on the best model to be used to estimate the geoid height. Presently, GEM-T1 (Marsh et al., 1988) and OSU86F would be most suitable. However, the decision of which model to use should be delayed as long as possible to allow use of the most accurate geoid.*

3) *The expected accuracy of the marine geoid at scales shorter than about 1500 km determined from altimetric data and gravity measurements will not be adequate for determination of the permanent global ocean circulation at these length scales. Consequently, a dedicated gravity mission should be flown as soon as possible (TOPEX Science Working Group, 1981). Such a mission is now being pursued jointly between the U.S. and several European countries.*

4) *The interpolation method used to obtain geoid estimates at the satellite measurement locations should be carefully considered and tested.*

5) *Quantify the errors of model geoids. The error description should go beyond the usual rms description to include wavenumber and geographical dependencies.*

6.4 Precision Orbit Determination

Accurate measurements of the height $h_g + h_d$ (Fig. 1) of the sea surface relative to a reference ellipsoid approximation to the earth's surface require accurate estimates of the height H of the satellite. The methods of precision orbit determination (POD) presently and soon-to-be in use are summarized in Sec. 2.6.4. The major source of orbit height error is due to errors in modeling the spacecraft orbit introduced by uncertainty in the earth's gravitational field. As noted in Sec. 6.3, major gravity field improvement efforts are underway in the U.S. and Europe. These activities have already resulted in a substantial improvement in the gravity field and geoid model. Other modeling errors which degrade the accuracy of H are uncertainties in spacecraft drag, solar radiation pressure, and earth radiation pressure (including albedo and atmospheric infrared transmittance). Additional errors are introduced by uncertainties in atmospheric refraction, ground station coordinates, solid earth and ocean tides, and antenna and retroreflector focal point locations.

Precision orbit determination teams have been formed for all three altimeters currently scheduled for launch in the early 1990s (TOPEX, POSEIDON and ERS-1). In addition to improvements in orbit modeling and assimilation of tracking data, a major activity of these teams is intercomparison of software systems (GEODYN at GSFC, UTOPIA at the University of Texas, and ZOOM at CNES). The activities of these teams are well documented and it is generally believed that adequate planning has taken place and resources allocated to ensure achievement of POD goals for all three projects. However, it must be remembered that unprecedented accuracy is being sought for these future altimetric missions. For TOPEX/POSEIDON, the goal is an accuracy of 13 cm in the radial ephemeris H. Achievement of this goal will be difficult.

Recommendations

1) *Experience with GEOSAT data has shown that changing to an improved geoid model in POD can introduce abrupt jumps in time series of sea surface elevation deduced from altimetric data (Cheney, personal communication). The geoid model used in POD must therefore either be the same throughout an altimeter mission, or all orbits from the beginning of the mission must be recomputed each time an improved geoid model is implemented in POD. The latter choice would certainly lead to confusion from multiple versions of data sets distributed to the scientific community.*

6.5 Height Bias Residual

After applying all of the corrections discussed in the previous sections, the altimeter range estimates must be validated by independent estimates of the altimeter height. Discrepancies between the altimeter range measurements and the calibration measurements are referred to as the height bias residual. Both TOPEX/POSEIDON and ERS-1 plan laser overflights to validate altimeter height measurement accuracy. The procedure is to measure simultaneously the satellite height with a laser while the altimeter measures the distance from the satellite to the ocean surface.

The most limiting factor in laser ranging is that laser pulses cannot penetrate clouds. The calibration site must therefore be chosen carefully. Typical cloud cover over most of the ocean is about 50%, which severely limits the laser tracking success rate. Another difficulty is that the laser optical center relative to the mean ocean surface in the altimeter footprint must be measured very accurately. This requires highly accurate leveling of the laser and tide gauge, and consideration of the spatial separation of the tide gauge and the altimeter footprint. To achieve centimeter accuracy in laser ranging, it is also important to know the relative locations of the altimeter antenna and laser retroreflector focal points on board the satellite. Another potential problem is the method of smoothing and interpolation or extrapolation of the altimeter measurement to the laser site. This problem could be eliminated by replacing island calibration sites with tower platforms in the open ocean. Alternatively, this problem could be resolved with the use of the two GPS receivers, one at the laser site and one at sea in the altimeter footprint.

For ERS-1, a network of lasers is proposed to reduce determination of the spacecraft height to a geometric measurement. In addition, an attempt will be made to eliminate as many geophysical effects as possible from the problem. Nighttime passes will be used to eliminate ionosphere refraction, and the calibration sites have been chosen to be low sea-state areas to minimize electromagnetic bias, skewness bias, and tracker bias. It is not clear that it is desirable to select a calibration site by these criteria. Effectively, this limits validation of the range measurements to only ideal conditions. It will not test the accuracies of the ionospheric range delay (Sec. 2.3.3) or the EM bias correction (Sec. 2.5.2).

Recommendations

1) *All factors affecting the quality of island-based calibration data should be carefully considered before selecting a calibration site. These factors include: prevailing weather conditions (clear skies are required for laser ranging), physical size of the island (which may contaminate the altimeter footprint), physical separation of the laser site and the tide gauge, physical separation of the tide gauge and the altimeter footprint, bathymetry in the vicinity of the tide gauge and altimeter footprint, and the smoothness of the marine geoid near the calibration site.*

2) *It would be advantageous to choose a calibration site that will experience a wide range of environmental conditions (e.g., atmospheric pressure, water vapor, wave heights) so that the accuracies of all of the corrections applied to the altimeter range estimates can be tested.*

3) *The usefulness of tower overflights and GPS receivers as alternatives to island-based calibration should be further evaluated. Potential advantages of towers are the elimination of questions about land contamination in the altimeter footprint and reduced spatial separation between the tide gauge and the altimeter footprint.*

4) *The feasibility of using an aircraft carrying a laser and GPS receiver to underfly the satellite for altimeter calibration should be investigated.*

5) *The height bias residual should be validated continuously throughout the altimeter mission to monitor altimeter performance. Limiting the validation to a period at the beginning of the mission precludes the possibility of determining any drifts in calibration.*

6) *NASA and CNES calibration data for TOPEX/POSEIDON should be exchanged.*

REFERENCES

Alishouse, J.C., 1983: Total precipitable water and rainfall determinations from the SEASAT scanning multichannel microwave radiometer. *J. Geophys. Res.*, **88**, 1929–1935.

Barrick, D.E., 1974: Wind dependence of quasi-specular microwave scatter. *IEEE Trans. Anten. Propag.*, **AP-22**, 135–136.

Barrick, D.E., and C.T. Swift, 1980: The SEASAT microwave instruments in historical perspective. *IEEE J. Oceanic Eng.*, **OE-5**, 74–79.

Barrick, D.E., and E. Bahar, 1986: Seasat microwave altimeter measurement of the ocean gravity wave equilibrium-range spectral behavior using full-wave theory. *Proc. IGARSS-86 Sympos.*, ESA Publ. Div., Ref. ESA SP-254, August 1986.

Born, G.H., M.A. Richards, and G.W. Rosborough, 1982: An empirical determination of the effects of sea-state bias on the SEASAT altimeter. *J. Geophys. Res.*, **87**, 3221–3226.

Brink, K.H., 1978: A laboratory study of open ocean barometric response. *Dyn. Atmos. and Oceans*, **2**, 153–183.

Brown, G.S., 1977: The average impulse response of a rough surface and its applications. *IEEE Trans. Anten. Propag.*, **AP-25**, 67–74.

Brown, G.S., 1979: Estimation of surface wind speeds using satellite-borne radar measurements at normal incidence. *J. Geophys. Res.*, **84**, 3974–3978.

Brown, G.S., H.R. Stanley, and N.A. Roy, 1981: The wind speed measurement capability of spaceborne radar altimetry. *IEEE J. Oceanic. Engin.*, **OE-6**, 59–63.

Brown, R.A., and G. Levy, 1986: Ocean surface pressure fields from satellite-sensed winds. *Mon. Wel. Rev.*, **114**, 2197–2206.

Callahan, P.S., 1984: Ionospheric variations affecting altimeter measurements: a brief synopsis. *Mar. Geod.*, **8**, 249–263.

Chang, A.T.C., and T.T. Wilheit, 1979: Remote sensing of atmospheric water vapor, liquid water, and wind speed at the ocean surface by passive microwave techniques from the Nimbus-5 satellite. *Radio Sci.*, **14**, 793–802.

Chang, H.D., P.H. Hwang, T.T. Wilheit, A.T.C. Chang, D.H. Staelin, and P.W. Rosenkranz, 1984: Monthly distribution of precipitable water from the Nimbus-7 SMMR data. *J. Geophys. Res.*, **88**, 5328–5334.

Chelton, D.B., and P.J. McCabe, 1985: A review of satellite altimeter measurement of sea surface wind speed: with a proposed new algorithm. *J. Geophys. Res.*, **90**, 4707–4720.

Chelton, D.B., and F.J. Wentz, 1986: Further development of an improved altimeter wind speed algorithm. *J. Geophys. Res.*, **91**, 14,250-14,260.

Chelton, D.B., K.J. Hussey, and M.E. Parke, 1981: Global satellite measurements of water vapour, wind speed and wave height. *Nature*, **294**, 529–532.

Chelton, D.B., E.J. Walsh, and J.L. MacArthur, 1988: Pulse compression and sea level tracking in satellite altimetry. *J. Atmos. and Oceanic Technol.,* (in press).

Cheney, R.E., and J.G. Marsh, 1981: SEASAT altimeter observations of ocean dynamic topography in the western North Atlantic. *J. Geophys. Res.,* **86**, 473–483.

Crepon, M.R., 1976: Sea level, bottom pressure, and geostrophic adjustment. *Memoires Soc. Royale des Sciences de Liege,* **6**, 43–60.

Davies, K., 1980: Recent progress in satellite radio beacon studies with particular emphasis on the ATS-6 radio beacon experiment. *Space Sci. Rev.,* **25**, 357–430.

Davies, K., G.K. Hartman, and R. Leitinger, 1977: A comparison of several methods of estimating the columnar electron content of the plasmasphere. *J. Atmos. and Terrest. Phys.,* **39**, 571–580.

Dobson, E.B., F. Monaldo, J. Goldhirsh, and J. Wilkerson, 1987: Validation of GEOSAT altimeter derived wind speeds and significant wave heights using buoy data. *J. Geophys. Res.,* **92**, 10,719–10,732.

Doodson, A.T., 1922: The harmonic development of the tide-generating potential. *Proc. Roy. Soc. London, Ser. A,* **100**, 305329.

Douglas, B.C., and R.W. Agreen, 1983: The sea-state correction of GEOS-3 and SEASAT altimeter data. *J. Geophys. Res.,* **88**, 32543260.

Francis, E.A., 1987: Calibration of the Nimbus-7 Scanning Multichannel Microwave Radiometer (SMMR). Master's thesis, Oregon State University, 248 pp.

Ginzburg, V.L., 1964: *The propagation of electromagnetic waves in plasmas.* Addison-Wesley Publishing Co.

Goldhirsh, J., 1983: Rain cell size statistics as a function of rain rate for attenuation modeling. *IEEE Trans. Anten. Propag.,* **AP-31,** 799–801.

Grody, N.C., 1976: Remote sensing of atmospheric water content from satellites using microwave radiometry. *IEEE Tran&. Anten. Propag.,* **AP-24,** 155–162.

Harrison, J.C., 1984: *Earth Tides (Benchmark Papers in Geology),* Hutchinson Ross, Pennsylvania.

Hayne, G.S., 1980: Wallops waveform analysis of SEASAT-1 radar altimeter data. NASA Contractor Report CR-15689, Applied Science Associates.

Hayne, G.S., and D.W. Hancock, 1982: Sea-state related altitude errors in the SEASAT radar altimeter. *J. Geophys. Res.*, **87**, 3227–3231.

Hayne, G.S., and D.W. Hancock, 1987: Waveform analysis for GEOSAT day 96. *Johns Eopicins APL Tech. Dig.*, **8**, 255–959.

Jackson, F.C., W.T. Walton, B.A. Walter, and C.Y. Peng, 1988: Sea surface mean square slope from Ku-band backscatter data. *J. Geophys. Res.*, (submitted).

Jorgensen, P.S., 1984: Navstar/Global Positioning System 18-satellite constellations. In *Navigation*, Vol II, The Institute of Navigation, Washington D.C., pp. 1–12.

Liu, W.T., 1984a: The effects of variations in sea surface temperature and atmospheric stability in the estimation of average wind speed by SEASAT SASS. *J. Phys. Oceanogr.*, **14**, 399–401.

Liu, W.T., 1984b: Estimation of latent heat flux with SEASAT SMMR, a case study in the north Atlantic. In: *Large-scale Oceanographic Experiments and Satellites*, Edited by C. Gautier and M. Fieux, pp. 205–221.

Lorell, J., E. Colquitt, and R.J. Anderle, 1982: Ionospheric correction for SEASAT altimeter height measurements. *J. Geophys. Res.*, **87**, 3207–3219.

MacArthur, J.L., P.C. Marth, and J.G. Wall, 1987: The GEOSAT radar altimeter. *Johns Hopkins A.P.I. Tech. Digest*, **8**, 176–181.

Marsh, J.G., (and 19 other authors), 1988: A new gravitational model for the earth from satellite tracking data: GEM-T1. J. *Geophys. Res.*, **93**, 6169–6215.

Maul, G.A., 1985: *Introduction to Satellite Oceanography*. Martinus Nijhoff Publishers, 606 pp.

Mazzega, P., 1985: M2 model of the global ocean tide derived from SEASAT altimetry. *Mar. Geod.*, **9**, 335–363.

Melchoir, P., 1983: *The Tides of the Planet Earth*, Pergamon Press, Oxford.

Mohan, S.N., G.J. Bierman, N.E. Hamata, and R.L. Stavert, 1980: SEASAT orbit refinement for altimetry application. *J. Astronaut. Sci.*, **28**, 405–417.

Mognard, N.M., and B. Lago, 1979: The computation of wind speed and wave heights from GEOS-3 data. *J. Geophys. Res.,* **84**, 3979–3986.

Monaldo, F., 1988: Expected differences between buoy and radar caltimeter estimates of wind speed and sign)ficant wave height and their implications on buoy-altimeter comparisons. J. *Geophys. Res.*, **93**, 2285–2302.

Moore, R.K., and A.K. Fung, 1979: Radar determination of winds at sea. *Proc. IEEE,* **67**, 1504–1521.

Parke, M.E., 1982: O1, P1, N2 models of the global ocean tide on an elastic earth plus surface potential and spherical harmonic decompositions for M2, S2, and K1. *Mar. Geod.,* **6**, 35–81.

Parke, M.E., and M.C. Hendershott, 1980: M2, S2, K1 models of the global ocean tide on an elastic earth. *Mar. Geod.,* **3**, 379–408.

Parke, M.E., R.H. Stewart, D.L. Farless, and D.E. Cartwright, 1987: On the choice of orbits for an altimetlic satellite to study ocean circulation and tides. *J. Geophys. Res.*, **92**, 11,693–11,707.

Platzman, G.W., G.A. Curtis, K.S. Hansen, and R.D. Slater, 1981: Normal modes of the world ocean, part 2: Description of modes in the period range 8 to 80 hours. *J. Phys. Oceanogr.*, **11**, 579–603.

Resch, G.M., 1984: Water vapor radiometers in geodetic applications. In *Geodetic Refraction,* edited by F.K. Brunner, Springer-VerLag, New York.

63

Rodriguez, E., 1988: Altimetry for non-Gaussian oceans: height biases and estimation of parameters. *J. Geophys. Res., (in* press).

Rodriguez, E., and B. Chapman, 1988: Extracting ocean surface information from altimeter returns: the deconvolution method. *J. Geophys. Res.*, (submitted).

Rush, C.M., 1986: Ionospheric radio propagation models and predictions—a mini review. *IEEE Trans. Anten. Propag.*, **AP-34**, 1163–1170.

Saastamoinen, J., 1972: Atmospheric correction for the troposphere and stratosphere in radio ranging of satellites. *Geophysical Monographs,* **15**, Amer. Geophys. Union, Washington D.C.

Sailor, R.V., and A.R. LeSchack, 1987: Preliminary determination of the GEOSAT radar altimeter noise spectrum. *Johns Hopkins APL Tech. Digest,* **8**, 182–183.

Schwiderski, E.W., 1980a: Ocean tides, Part I: Global ocean tidal equations. *Mar. Geod.*, **3**, 161–218.

Schwiderski, E.W., 1980b: Ocean tides, Part II: A hydrodynamical interpolation model. *Mar. Geod.,* **3**, 161–218.

Shawe, M.E., and A.G. Adelman, 1985: Precision laser tracking for global polar motion. *IEEE Trans. Geosci. Rem. Sens.*, **GE-23**, 391–397.

Skolnik, D.L., editor, 1970: *Radar Handbook,* McGraw-Hill Book Co.

Sloss, P.W., 1987: Global marine gravity field map. *Eos Trans. Amer. Geophys. Union,* **68**, 770, 772.

Smith, E.K., and S. Weintraub, 1953: The constants in the equation for atmospheric refractive index at radio frequencies. *Inst. Radio Eng.*, **41**, 1035–1037.

Soicher, H., 1986: Variability of transionospheric signal time delay at subauroral latitudes. *IEEE Trans. Anten. Propag.*, **AP-34**, 1313–1319.

Srokosz, M.A., 1986: On the joint distribution of surface elevations and slopes for a nonlinear random sea, with an application for radar altimetry. *J. Geophys. Res.*, **91**, 995–1006.

Staelin, D.H., K.F. Kunzi, R.L. Pettyjohn**,** R.K.L. Poon, R.W. Wilcox, and J.W. Waters, 1976: Remote sensing of atmospheric water vapor and liquid water with the Nimbus-5 microwave spectrometer. J. *Appl. Meteor.*, 15, 1204–1214.

Stanley, H.R., 1979: The GEOS-3 Project. J. *Geophys. Res.*, 84, 3779–3783.

Stewart, R.H., 1985: *Methods of Satellite Oceanography.* Univ. Calif. Press, Berkeley, Calif., 360 pp.

Tapley, B.D., and G.H. Born, 1980: The SEASAT precision orbit determination experiment. *J. Astronaut. Soc.*, **28**, 315–326.

Tapley, B.D., G.H. Born, and M.E. Parke, 1982a: The SEASAT altimeter data and its accuracy assessment. *J. Geophys. Res.*, **87**, 3179–3188.

Tapley, B.D., J.B. Lundberg, and G.H. Born, 1982b: The SEASAT altimeter wet tropospheric range correction. *J. Geophys. Res.,* **87***,* 3213–3220.

TOPEX Science Working Group, 1981: Satellite altimetric measurements of the ocean. Doc. 400-111, Jet Propul. Lab., Pasadena, Calif.

Townsend, W.F., 1980: An initial assessment of the performance achieved by the SEASAT altimeter. *IEEE J. Oceanic Eng.,* **OE5**, 80–92.

Trenberth, K.E. , and J. G. Olson, 1988: Intercomparison of NMC and ECMWF global analyses: 1980–1986. *NCAR Tech. Note,* NCAR/TN-301+STR, 81 pp.

Ulaby, F.T., T.F. Haddock, and R.T. Austin, 1988: Fluctuation statistics of millimeterwave scattering from distributed targets. *IEEE Trans. Geosci. Rem. Sens.,* **26**, 268–281.

Varghese, T., V. Husson, S.Wetzel, J.Degnan, and T.Zagwodzki, 1988: Intercomparison of satellite laser ranging accuracy of three NASA stations through collocation. In: *Acquisition, Tracking and Pointing II,* Soc. Photo-Optical Instr. Eng., Vol. 881.

Walsh, E.J., 1979: Extraction of ocean wave height and dominant wavelength from GEOS-3 altimeter data. *J. Geophys. Res.,* **84**, 4003–4010.

Walsh, E.J., 1982: Pulse-to-pulse correlation in satellite radar altimeters. *Radio Sci.,* **17***,* 786–800.

Walsh, E.J., F.C. Jackson, E.A. Uliana, and R.N. Swift, 1988: Observations on electromagnetic bias in radar altimeter sea surface measurements. *J. Geophys. Res., (*submitted).

Wentz, F.J., 1982: A model function for ocean microwave brightness temperature. *J. Geophys. Res.,* **88**, 1892–1908.

Wentz, F.J., L.A. Mattox, and S. Peteherych, 1986: New algorithms for microwave measurements of ocean winds: applications to SEASAT and SSM/I. *J. Geophys. Res.,* **91**, 2289–2307.

Wilheit, T.T., A.T.C. Chang, M.S.V. Rao, E.B. Rodgers, and J.S. Theon, 1978: A satellite technique for quantitatively mapping rainfall rates over the ocean. *J. Appl. Meteor.,* **l6**, 551–560.

Wilmes, H., C. Reigber, W. Schafer, and P. Hartl, 1987: Precise Range and Range-rate Equipment, PRARE, on-board ERS-1. In: *Proceedings of the XIX IUGG General Assembly, Vancouver, 1987, Vol. II*, pp. 586–596.

Witter, D.L., and D.B. Chelton, 1988: Estimation of temporal variability of sea-state bias in altimeter height measurements. *J. Geophys. Res.,* (submitted).

Woodworth, P.L., and D.E. Cartwright, 1986: Extraction of the M2 ocean tide from SEASAT altimeter data. *Geophys. J. Roy. Astro. Soc.*, **84**, 227–255.

Wunsch, C., 1972: Bermuda sea level in relation to tides, weather, and baroclinic fluctuations. *Rev. Geophys. Space Phys.,* **10**, 1–49.

Yunck, T.P., S.C. Wu, and S.M. Lichten, 1985: A GPS measurement system for precise satellite tracking and geodesy. *J. Astronaut. Soc.*, **33**, 367–380.

LIST OF WORKSHOP ATTENDEES

David Adamac
Inst. for Naval Oceanogr.
Bldg 1100 Rm 205
NSTL, MS 39529-5005
601-688-5737

Yehuda Agnon
Massachusetts Inst. of Tech.
Dept. of Mathematics
Bldg. 2-335
Cambridge, MA 02139
617-253-7905

P.A.M. Berry
Universty of Leicester
University Rd.
Leicester, Leisre
UNITED KINGDOM
0533-552079

Richard Biancale
CNES/GRGS
18 Avenue E. Belin
31055 Toulouse Cedex
France
61274124

George Born
University of Colorado
Dept. of Aerospace Engr.
C.B. 431
Boulder, CO 80309
303-492-8638

Claude Brossier
CNES/GRGS
18 Ave. Ebelin
31055 Toulouse Cedex
France
33-66274417

Philip S. Callahan
Jet Propulsion Lab.
4800 Oak Grove Dr.
Mail Stop T-1206D
Pasadena, CA 91109
818-354-4753

Jack Calman
Johns Hopkins Univ./APL
Johns Hopkins Rd.
Laurel, MD 20707
301-953-5000 x4398

Dudley B. Chelton
College of Oceanography
Oregon State University
Corvallis, OR 97331
503-754-4017

Robert Cheney
NOAA/Natl. Ocean Service
Code N-CG 11
Rockville, MD 20852
301-443-8556

Edward J. Christensen
Jet Propulsion Lab.
4800 Oak Grove Dr.
Pasadena, CA 91109
818-354-1992

K. Danas
Deutsches Geodatisches
Forschungsinstitut (DGFI)
Marstallplatz, 8
D-8000 MUNCHEN 22
Federal Republic GERMANY
305-361-4018

Roland DeSzoeke
College of Oceanography
Oregon State University
Corvallis, OR 97331
503-754-3160

Ella B. Dobson
Johns Hopkins Univ.
Applied Physics Lab
Johns Hopkins Road
Laurel, MDF 20707
301-953-5000 x8645

Michel Dorrer
CNES
18 Ave Edouard Belin
31055 Toulous Cedex
FRANCE

Theodossios Engelis

1958 Neil Ave.
Ohio State University
Dept. Geodetic Sci. & Surveying
Columbus, Ohio 43210
614-292-6753

Philippe Escudier
CNES SCM/ESM/TP
18 Av. Edouard Belin
31055 Toulous Cedex
FRANCE
61 273486

Dr. Robert Evans
University of Miami
Rosenstiel School of
Marine & Atmos. Sci.
4B00 Rickenbacker Cswy.
Miami, FL 33149
305-361-4018

Pierre Flament
Woods Hole Oceanogr. Inst.
Clark-3
Woods Hole, MA 02543
617-548-1400 x2781

Ed Flinchem
School of Oceanography
University of Washington
Seattle, WA 98195
206-543-0766

M. C. Forbes
University of Miami
RSMAS
4600 Rickenbacker Cswy.
Miami, FL 33149
305-361-4038

Ron Forsythe
NASA
GSFC/WFF
Wallops Island, VA 23337
804-824-1357

Richard Francis
ESA/ESTEC
Section ORM
Keplerlaan 1
2200 AG Noordwijk
THE NETHERLANDS
+.31.1719.84460

Michael Freilich
Jet Propulsion Lab
Mail Stop 169-236
4800 Oak Grove Dr.
Pasadena, CA 91109
818-393-7801

Lee-Lueng Fu
Jet Propulsion Lab.
4800 Oak Grove Dr.
Mail Stop 169-236
Pasadena, CA 91109
818-354-8167

Newell Garfield, III
Univ. Rhode Island
Grad. School of Oceanogr.
South Ferry Road
Narragansett, RI 02882
401-792-6101

Jim Gower
Inst. of Ocean Sciences
P.O. Box 6000
Sidney, B.C. V8L 4B2
CANADA
G04-356-6558

Hans C. Graber
Woods Hole Oceanogr. Inst.
Dept. of Ocean Eng.
Bigelow 105
Woods Hole, MA 02543
617-548-1400

Bruno Greco
ESA/Earthnet
via Galileo Galilei
Casella Postale 64
00044 Frascati, ITALY
+.39.6.94011

Trevor Guymer
Inst. of Oceanographic Sciences
Deacon Laboratory
Brook Road
Wormley, Godalming
Surrey GU8/5UB
ENGLAND
042879-4141

Bruce Hackett
VERITEC
Box 300
1322 Hovik
NORWAY
472-479621

David W. Hancock
NASA/GSFC
Wallops Flight Facility
Wallops Island, VA 23337
804-824-1238

George Hayne
NASA/GSFC
Wallops Flight Facility
Wallops Island, VA 23337
804-824-1294/2526

Frederick C. Jackson
NASA/GSFC
Code 671
Greenbelt, MD 20771
301-286-5380

Steve Keihm
6805 N. Rosemead Blvd. #28
San Gabriel, CA 91775
818-287-7216

Steve Klosko
EG & G
5000 Philadelphia Way
Suite J
Lanham, MD 20706
301-731-2044

Chester Koblinsky
Code 621
NASA/GSFC
Greenbelt, MD 20771
301-286-2880

Ron Kolenkiewicz
NASA/GSFC
Code 621
Greenbelt, MD 20771
301-286-5373

Gary Lagerloef
SAIC
13400B Northrup Way, NE
Suite 36
Bellevue, WA 98005
206-747-7152

Steve Lingsch
Inst. for Naval Oceanogr.
Bldg 1100 Rm 205
NSTL, MS 39529-5005
601-688-3518

John MacArthur
Johns Hopkins Univ.
Applied Physics Lab.
Johns Hopkins Rd.
Laurel, MD 20707
301-953-6411

Chreston Martin
EG & G WASC
5000 Philadelphia Way
Suite J
Lanham, MD 20706
301-731-2044

Yves Menard
CNES/GRGS
18 Ave. E Belin
31055 Toulouse Cedex
FRANCE
61-274011

Alberto Mestas-Nunez
College of Oceanography
Oregon State University
Corvallis, OR 97331
503-753-9980

Jean-Francois Minster
CNES-GRGS
18 Avenue Edward Beline
31055 Toulouse Cedex
FRANCE
6127 3935

Nelly M. Mognard
University of Pudget Sound
USGS Ice and Climate Project
Tacoma, WA 98416
206-383-7944

Frank M. Monaldo

Johns Hopkins Univ./APL
Johns Hopkins Road
Laurel, MD 20707
301-953-5000 x8648

Jeff Paduan
College of Oceanography
Oregon State University
Corvallis, OR 97331
503-754-4548

Michael Parke
Jet Propulsion Lab
Mail Stop 169-236
4800 Oak Grove Dr.
Pasadena, CA 91109
818-354-2739

Dr. Steven Patterson
NOAA/NODC
Code E/OC11
1825 Connecticut Ave. NW
Washington, D.C. 20235
202-673-5601

Philippe Raizonville
CNES
18 Ave. Edouard Belin
31055 Toulouse Cedex
FRANCE
61273047

James Richman
Oceanic Processes Branch
NASA Headquarters
Code EEC
Washington, D.C. 20546
202-453-1725

Michelle Rienecker
Inst for Naval Oceanography
Bldg. 1100 Rm 205
NSTL, MS 39529-5005
601-688-5737

Ernesto Rodriguez
Mail Stop T-1206D
Jet Propulsion Lab
4800 Oak Grove Dr.
Pasadena, CA 91109
818-354-2647

Ernst W. Schwiderski
Naval Surface Weapons Center
Code K104
Dahlgren, VA 22448-5000
703-663-8454

Frank Sciremammano
Rochester Inst. of Tech.
Dep. of Mech. Eng.
One Lomb Drive
Rochester, NY 14623
716-475-6819
716-475-2162

Joe Shuhy
NRL, Code 8315,5
Washington, D.C. 20375
202-767-2778

Dr. C. K. Shum
University of Texas
Center for Space Research
WRW 402, UT
Austin, TX 78712
512-471-5573

Scot Smith
Civil Eng. Dept.
Ohio State University
2070 Neil Ave.
Columbus, OH 43210
614-292-6889

Meric Srokosz
British National Space Centre
Building R 16
Royal Aircraft Establishment
Farnborough, Hants GU14 6TD
GREAT BRITAIN
0252-522822

Robert Stewart
A-030
Scripps Inst. of Oceanogr.
La Jolla, CA 92093
619-534-2140
818-353-3327

Ted Strub
College of Oceanography
Oregon State University
Corvallis, OR 97331

503-754-3015

Chang-Kou Tai
Scripps Inst. of Oceanogr.
Ocean Research Division
SIO A-030
La Jolla, CA 92093
619-534-6358

Al Uliana
Naval Research Lab
Code 8312
Washington, D.C. 20375
202-767-3185

Edward Walsh
(NASA), R/E/WP
NOAA/ERL Wave Propagation Lab.
325 Broadway
Boulder, CO 80303
303-497-6357

Frank Wentz
Remote Sensing Systems
1101 College Ave, Suite 220
Santa Rosa, CA 95404
707-545-2904

W. Stanley Wilson, Chief
Oceanic Processes Branch
NASA Headquarters
Code EE-C
Washington, D.C. 20546
202-453-1725

Duncan Wingham
Univ. College of London
Gower Street
London WCIE 7JE
UNITED KINGDOM
01-387-7050 x3197

Victor Zlotnicki
Jet Propulsion Lab.
4800 Oak Grove Dr.
Mail Stop 169-236
Pasadena, CA 91109
818-354-5519